Design and Validation of a 2-DoF Force-Controlled Finger Skin Stretch Device for Hand Rehabilitation

RO57035: RO MSc Thesis

Rubén Martín Rodríguez

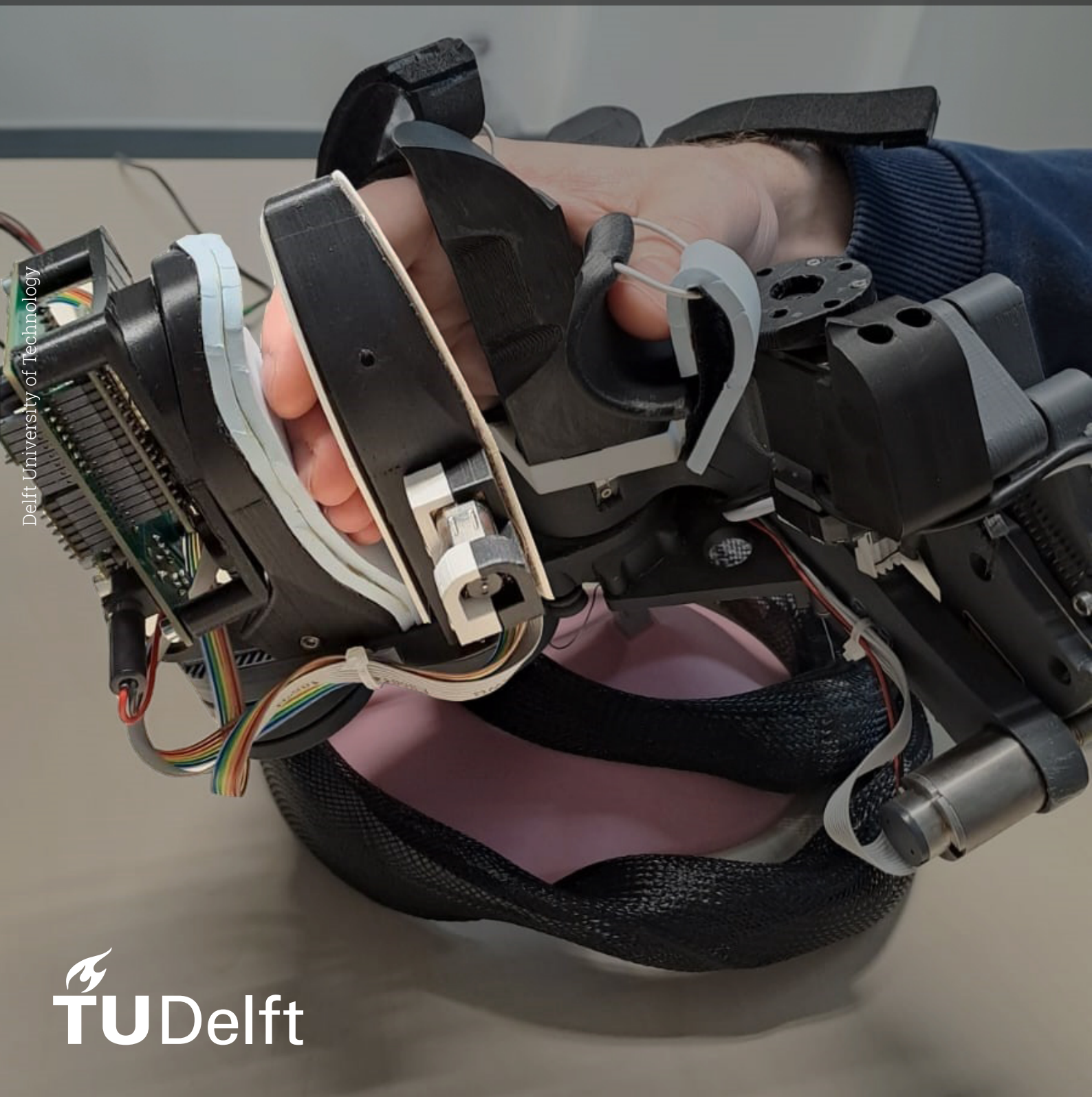

Delft University of Technology

TU Delft

Design and Validation of a 2-DoF Force-Controlled Finger Skin Stretch Device for Hand Rehabilitation

by

Rubén Martín Rodríguez

to obtain the degree of

Master of Science
in Robotics

At the:
Department of Cognitive Robotics,
Delft University of Technology,
to be defended on November 30th, 2023 at 10:15 AM.

Student number: 5507391

Thesis committee:

Dr. Ing. L. Marchal-Crespo	TU Delft, main supervisor, chair
Dr. Y. Vardar	TU Delft, supervisor
A.L. Ratschat	TU Delft, daily supervisor
Dr. M. Wiertlewski	TU Delft, external committee member
Dr. Ir. A.H.A Stienen	TU Delft, external committee member

An electronic version of this thesis is available at http://repository.tudelft.nl/.

TU Delft

Preface

I am greatly excited to present in this document the result of what has been, over the last nine months, not only my full-time work but also the catalyzer of one of my greatest learning experiences. I look back at where this project started, with the left-hand unit of the hand rehabilitation robot just assembled and ready for modification, and a whole list of ideas, designs, and experiments that I could make. Yet, as is often the case with these projects, the final result is one I could have never imagined.

I am very happy to have been able to carry out a project like this, allowing me to touch upon so many aspects and dimensions of engineering, and to design and create such a device (even a force sensor!). The journey has not been easy, with frustration because components broke, designs didn't work and some implementations would take days or weeks. However, it has come with an equal amount of celebratory moments and excitement as things took shape. I believe it all has allowed me to grow not only in technical skills but also in my way of thinking and organizing my time, as well as shedding light on the kind of work I want to pursue in my future. For that, I am glad I went to talk with Prof. Laura Marchal-Crespo after her lecture in the Human-Robot Interaction course, now almost two years ago.

Of course, this achievement would have been impossible without the assistance of many people. First and foremost, I want to express my most sincere gratitude to my supervisors: Alexandre Ratschat, Yasemin Vardar, and Laura Marchal-Crespo. Your detailed feedback, assistance, and guidance have been invaluable. I would also like to extend my gratitude to all the members of the MLN Lab, some of whom have graduated or moved abroad, the many others who have joined, and those who have accompanied me all throughout the thesis. The ideas and discussions we have exchanged, and the coffee and lunch breaks we have shared, have helped immensely along the way. It has been a pleasure to be part of this group and to have occupied for this last year before moving, that one desk at the end of the VR room. I would also like to thank all those who have assisted this project in taking shape, by sharing their ideas, equipment, and materials.

Finally, I could have not achieved this project without the endless support of my father and my girlfriend, even while far away from me. You have been my emotional support, keeping me afloat when I most needed it. Also to my flatmates and friends in the Netherlands, for all the good times we have shared and that have allowed me to unwind from the project and replenish my energies. And thank you, mum, I know you are always cheering and encouraging me with the grandpas from up above, I could have never gotten here without you.

Rubén Martín Rodríguez
Delft, November 2023

Contents

1

Introduction

The body of this thesis is built around the paper ”Design and Validation of a 2-DoF Force-Controlled Finger Skin Stretch Device for Hand Rehabilitation” in Chapter 2. This includes the majority of the research and the main findings of the thesis. For further information, the author would like to refer the reader to the included appendices.

Additional notes on the design of the interface can be found in Appendix A. A summary of the requirements is included, in addition to calculations and intermediate outputs that led to the final design of the interface. The complete bill of materials is also included. The schematics and design of the Printed Circuit Boards (PCBs) developed throughout the thesis can be found in Appendix B. The details on the manufacturing process of the components manufactured and assembled in-house are provided in Appendix C. Appendix D contains a description of the software architecture in the microcontroller, as well as the workflow of the different tasks and processes.

Regarding the validation of the system, a detailed description of the setups and scripts used to perform the measurements and tests is provided in Appendix E. In addition to the results presented in the paper, additional insights and visualizations are included in Appendix F.

Finally, Appendix G includes some of the technical drawings and technical documents generated throughout the thesis and which are discussed throughout the appendices.

2

Paper: Design and Validation of a 2-DoF Force-Controlled Finger Skin Stretch Device for Hand Rehabilitation

Design and Validation of a 2-DoF Force-Controlled Finger Skin Stretch Device for Hand Rehabilitation

R. Martín Rodríguez
Supervised by: A.L. Ratschat, Y. Vardar, and L. Marchal-Crespo

***Abstract*—The provision of somatosensory information may play a fundamental role in the recovery of stroke patients. Particularly, tactile information is known to influence motor control by contributing to the perception of the weight, friction, and slip condition of objects. Despite this, the inclusion of tactile information through haptic rendering in robotic neurorehabilitation systems remains largely unexplored. In this study, we present a tactile interface to extend the kinesthetic rendering capabilities of an existing hand rehabilitation robot. The developed solution relies on skin stretch stimulation of the fingerpads, which allows the rendering of interaction forces with tangible virtual objects, e.g., friction, weight, and inertia. In contrast with previous skin stretch devices, our system uses closed-loop force control for accurate force rendering, relying on a custom magnetic field-based three-axis force sensor. A three-axis positioning stage in combination with a reference force sensor was used for calibrating and characterizing the sensor, as well as evaluating the interface response. The sensor achieves shear force accuracies of 0.2 N, influenced by hysteresis and viscoelastic creep effects. The tactile interface achieves a steady-state error of 0.2–0.4 N and rise times of 20–70 ms during step response tests. Frequency response tests show that the interface can successfully track signals up to 5–7 Hz. The novel use of force-controlled skin stretch stimulation aims to open a new avenue for the accurate rendering of interaction forces through the tactile sense. Moreover, through purposeful design for usage in the rehabilitation domain, we hope that this study will serve as a stepping stone toward the inclusion of tactile information in robot-assisted therapies.**

***Index Terms*—Haptic interfaces, neurorehabilitation, tactile feedback, magnetic force sensors, force control.**

Fig. 1. Tactile interface device developed in the present study, assembled into the hand rehabilitation robot by Rätz et al. [1]. The device, in contact with the fingerpads, provides force-controlled skin stretch stimulation, which allows for accurate rendering of tangential forces, like the weight or the friction forces, when interacting with a virtual tangible object.

I. Introduction

STROKE is listed as the second major cause of death globally, with over 12 million cases registered each year [2]. About 75% of stroke survivors present long-term hand impairments [3], which impact their performance and autonomy during daily life activities [4].

Neuroscience evidence suggests that high-intensity [5], task-specific training [6] is crucial to improve functional motor recovery after stroke. Sensory training has also been recommended [7] based on the evidence associating somatosensory impairment with reduced or prolonged motor recovery [8], [9]. However, the intensity and duration of the training are limited due to the endurance and availability of the therapists. Moreover, current therapies focus mostly on motor functions, neglecting the sensory side of the neurorehabilitation process [10].

Robotic systems have arisen as a possible means to provide high-intensity training [11] together with virtual reality (VR), which has been explored as a means to provide visual and auditory information in highly motivating and safe training environments [12]. However, to successfully manipulate tangible objects, it is crucial to perceive the properties of the object and the forces arising from the interaction. This information is gathered from the mechanoreceptors in our muscles, sensing the position of our body and the forces applied to it (kinesthetic information), and in our skin, allowing us to perceive material properties and interaction forces (tactile information) [13]. Robotic systems can convey such information, while assisting the patient, in the form of haptic rendering, that is, the provision of simulated forces and stimuli from the interaction with tangible virtual objects [11].

In particular, the tactile sense is known to provide information about object friction [14], weight [15], and slip condition [16], which ultimately influence the way humans manipulate and interact with objects [17]–[19]. However, when looking into robotic rehabilitation systems for the hand, the focus is typically placed on the provision of kinesthetic information

The author and supervisors are with the Department of Cognitive Robotics, Delft University of Technology, Delft, 2628 CN, Netherlands.

[20]. This narrow focus neglects the essential contribution of the tactile sense for motor control, leaving its inclusion in robot rehabilitation largely unexplored.

Within the broader field of haptics, on the contrary, there is a wide range of devices and technologies acting upon the tactile sense to render multiple sensations and stimuli [21]. A particular set of technologies relies on the induction of naturally occurring skin deformations to render interaction forces with tangible virtual objects. Such stimulation, when applied tangentially to the skin, is commonly referred to as skin stretch and is capable of rendering forces such as friction [22] or weight [23]. Considering the importance of these forces for object manipulation and motor control [24], [25], this type of stimulation can be a valuable addition to the rendering capabilities of rehabilitation robots.

Yet, when considering the inclusion of skin stretch devices into the rehabilitation domain, several limitations arise. For example, stroke patients often suffer from chronic hand and finger spasticity, preventing them from voluntarily opening their hands [26]. Thus, a wearable form factor, commonly found in existing skin stretch devices, would require external assistance to open the hand and mount the devices, making them cumbersome to use. Furthermore, high-fidelity rendering is required to promote the transfer of the gained skill in the virtual environment to the real physical world [27]. Skin stretch devices, however, typically render forces by applying a displacement computed through an estimate of the finger pad stiffness [28]–[30]. Considering the large variability in finger pad stiffness under varying pressure levels and across individuals [31], [32], the accuracy with which current devices render forces is, therefore, limited. Finally, most of these devices stimulate a single finger, requiring multiple units to achieve whole-hand stimulation [28]–[30].

A few studies have attempted to render forces through force-controlled skin stretch [33], [34]. To do so, a commercial 6-axis force-torque sensor was placed between the mechanism and the fingers to measure the rendered forces. However, the proposed systems constrain the hand position to a pinch grasp, stemming from the focus on psychophysics of the respective studies. Additionally, the limited workspace of the devices limited the range of movements of the user. Consequently, these systems are not suited for haptic rendering during the whole arm and hand motions involved in upper-limb rehabilitation [1], [11].

This study presents a novel tactile interface for 2-Degree-of-Freedom (DoF) force rendering via force-controlled skin stretch stimulation, attained through a custom miniature force sensor to achieve an inexpensive solution. The interface is designed to be integrated into the 3-DoF hand rehabilitation robot developed by Rätz et al. [1], [35] (see Figure 1). The proposed design strives for simple integration into the robot and extension of its haptic rendering capabilities with simultaneous multi-finger tactile stimulation.

The incoming sections present the design requirements, gathered through a review of the literature on psychophysics and object manipulation, together with the constraints imposed by its integration into the current robotic hand robot. The proposed design of the device and the integrated sensor are then presented, followed by a description of the apparatus employed to calibrate the sensor and validate the interface. Finally, the outcomes of the sensor performance are presented together with the results of the interface validation.

II. Methods

A. Requirements

The design and the selection of components have been driven by several constraints imposed by the robot in which the interface is mounted, as well as the requirements and desired capabilities of the tactile interface. Also, a low-cost solution was targeted due to the early-prototype nature of the project, as well as aiming for an inexpensive final result.

1) System-level constraints: The tactile interface is intended for integration into the Palmar RehabilitatIon DEvice (PRIDE) developed by Rätz et al. [1], whose key features should not be compromised by the inclusion of the interface. PRIDE is a robotic hand rehabilitation device supporting finger movement and providing haptic rendering during a cylindrical grasp motion [1]. The device features a palmar design for effortless setup of the hand in a closed position, physiological full finger flexion/extension for a large range of hand sizes, and high mechanical transparency for accurate haptic rendering. The device also supports thumb flexion/extension and circumduction [35], achieving whole-hand kinesthetic rendering.

In short, the robot actuates the four fingers from the index to the little finger simultaneously, from full extension to a 165° flexion [1], [35]. The thumb mechanism supports 0 – 65° flexion/extension and 0 – 80° circumduction [35]. These ranges of motion should remain as unaffected as possible. Furthermore, the modified system should continue to allow the setup of the hand in a closed position to allow for its use by patients with finger and hand spasticity.

To achieve whole-hand tactile stimulation, separate modifications would be needed to the finger and thumb mechanisms. The tactile interface proposed in this study targets the finger flexion/extension mechanism. This was decided based on the high importance of the motion, particularly of the index finger, for hand rehabilitation [1], as well as the large area that can be stimulated with the modification. Additionally, the integration of multi-finger skin stretch stimulation in a single device is largely unexplored, posing an additional challenge to address when introducing tactile stimulation in the device.

With that in mind, the tactile interface should actuate all four fingers and support similar hand and finger sizes as in the original finger flexion mechanism [1]. Because of this focus and the eventual need for modifications of the thumb actuation, the range of motion (ROM) of the fingers was prioritized over those of the thumb.

2) Device-level requirements: In addition to the constraints imposed by the overarching system, multiple requirements were gathered to define what the tactile interface should be capable of. These include the number of degrees of freedom, maximum actuation, temporal response, accuracy, and ROM.

The forces arising from object interaction and manipulation in free space are usually three-dimensional. While the hand rehabilitation robot is capable of rendering forces in the normal

direction to the fingerpads, actuation over the tangential plane is currently missing. To be capable of rendering forces over the entire plane, the skin stretch interface should be actuated in two degrees of freedom (2-DoF).

Regarding the magnitude of the forces, studies on force and weight perception have shown that kinesthetic information proves to be equivalent and even dominates over tactile information for forces over 2–3 N [33], [36]. However, the accuracy for discriminating the magnitude of forces and weights was always observed to improve with the addition of tactile information, even for larger values. Therefore, a maximum force of 5 N along each dimension should be targeted. This value also allows for the rendering of the weight and interaction forces with common objects. Furthermore, the interface should be capable of rendering those forces in a lapse of less than 0.35 s. This value was measured during object lifting experiments as the time needed for the lifting forces to match the weight of the object [24], [37].

Additionally, the device should provide a high-fidelity rendering of the interaction forces and achieve an accuracy below the just-noticeable difference (JND) for force perception. From the psychophysics literature, it is known that the JND is proportional to the absolute stimulus by a factor referred to as the Weber Fraction (WF) [38]. Typical estimates of this factor report a constant value of 9–12% or lower for forces over 1.5 N, depending on experimental conditions [39]. However, this factor has been observed to double and three-fold for smaller forces [38]–[40]. Overall, JND values as low as 50–100 mN are reported in the literature for weight perception under combined kinesthetic and tactile conditions [41]–[44], with larger values under unisensory conditions depending on the sensory channel and reference weight [33], [45]. Based on those findings, the interface should ideally exert forces with an accuracy of 50 mN for weights below 1.5 N, and 100 mN for larger values.

Finally, studies have reported deformations of the fingerpads as large as 5 mm in the mediolateral direction [31]. Therefore, the device should be capable of stretching the skin by deformations of a similar amount.

B. Design

1) Mechanical design: Based on the gathered requirements, the proposed tactile interface is designed as a replacement for the existing finger end-effector of the robot [1], which provides support for the fingers at the fingerpads. The tactile interface features a 2-DoF moving platform in contact with the fingerpads to attain actuation over the entire tangential plane.

To ensure that the platform movements cause a deformation of the fingerpads, existing skin stretch devices either ground the back of the finger on the device itself [23], [28], or rely on the pressure applied by the user [46]. Instead, the proposed design grounds the back of the finger on the quick-release finger fixation of the hand robot, as seen in Figure 1.

The platform actuation is inspired by the design of Preechayasomboon et al. [46], using a leadscrew connected to a brushed direct current (DC) motor. This approach features a low number of components; low-cost, simple, and compact

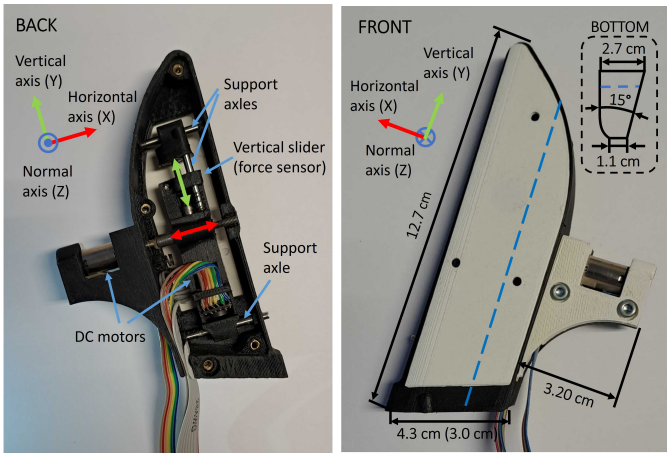

(a) (b)

Fig. 2. Design of the tactile interface. (a) Inside view of the interface from the back, showing the mechanism for actuating the moving platform. The actuator of the horizontal axis displaces the vertical axis along two supporting axles in the proximodistal direction of the hand. The vertical axis moves the platform in the mediolateral direction. (b) Front view of the interface with the corresponding dimensions. In the top-right corner, a schematic diagram of the bottom view of the interface is shown with associated dimensions. The diagram is rotated such that the bottom part corresponds to the left part of the picture. The blue lines indicate the original size of the finger end-effector of the hand rehabilitation robot along the modified dimension.

actuation; and consistent performance across the complete ROM. The proposed device, however, extends the actuation to 2-DoF through a serial mechanism with one axis in the proximodistal direction of the fingers (horizontal, or X, axis) and another in the mediolateral direction (vertical, or Y, axis), as depicted in Figure 2. Each axis consists of an actuated leadscrew assembly with supporting axles to provide stability to the platform movement. These axles are also needed to withstand the forces rendered by the robot in the normal direction (or Z axis) during grasping. In this configuration, each axis achieves a total ROM of ± 4.5 mm

To realize the leadscrew actuators, a pair of brushed DC motors (5:1 Micro Metal Gearmotor HPCB 6V with Extended Motor Shaft, Pololu, United States) are used. The proposed motors were estimated to provide sufficient torque to overcome the friction losses in the transmission while achieving the maximum actuation and temporal response targeted. A conventional M3x30 mm stainless steel threaded rod with 0.5 mm lead is used as a leadscrew, and an M3x5.8 mm brass insert (M3-UHBRHESF, TR Fastenings, United Kingdom) is selected as the screw nut. The threaded rod is attached to the motor through a custom coupler manufactured in-house. The support axles of each axis are manufactured from 3 mm diameter stainless steel shafts. To minimize friction in the axles, the parts sliding over each horizontal axle feature a miniature linear bearing (C-LMU3, MISUMI Europe, Germany). A Teflon insert is used for the sliding part in the vertical axis due to size constraints and improved performance in preliminary tests.

A set of custom 3D-printed parts make up the housing of the device and provide connections for the actuators and the mechanical components. The parts were manufactured

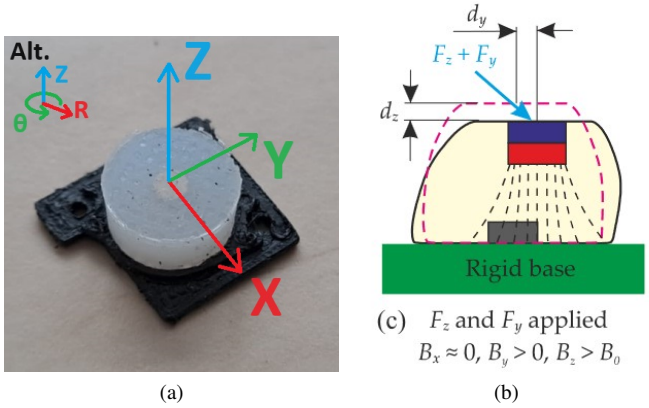

(a) (b)

Fig. 3. (a) Fully manufactured unit of the elastomer with an embedded magnet for the custom force sensor. The three main measurement axes are overlaid on top of the elastomer. The cylindrical coordinate frame depicted at the top-left corner was the one used for generating the deformations applied during the calibration. (b) Diagram illustrating the magnetic-field-to-force transducing mechanism of the sensor. Adapted from Wang et al. [47] (license: CC-BY 4.0, cropped from original).

using FDA-approved 3D-printing filament (GreenTEC anthracite/GreenTEC white, Extrudr, Austria).

2) Force sensor: To accurately render forces through the skin stretch interface, a sensor measuring the forces applied to the fingerpads is needed. To do so, the sensor should be as close as possible to the force application point, that is, between the moving component of the vertical axis of the interface and the platform in contact with the fingers (see Figure 2). Such a location allows the measurement of the applied forces without the influence of the friction and damping forces inherent to the mechanism. Yet, this limits the sensor size to a volume of approximately $1\,\mathrm{cm}^3$. Such tight size constraints, together with the low-cost requirement for the interface, prevented the use of a commercial multi-axis force sensor.

We, therefore, opted for manufacturing a custom magnetic-field-based force sensor [47]–[49]. This type of sensor relies on a magnet embedded in an elastomer. When forces are applied, the elastomer deforms and causes the magnet to displace (see Figure 3b). The variations in the magnetic field due to these displacements are measured through a three-axis magnetometer located at the base of the elastomer, a certain distance, or *air gap*, beneath the magnet. Through a calibration procedure, the sensor can measure the applied forces based on the variations in the magnetic field.

Magnetic-field-based force sensors feature good adaptability to different requirements by carefully selecting the material and shape of the elastomer in which the magnet is embedded [47]. Additionally, the manufacturing process is simpler and cheaper than other multi-axis force-sensing systems, such as those based on strain [50] or capacitive sensing [51]. Because magnetic-field-based sensors rely on displacements of the magnetic field under applied forces, one disadvantage is the presence of errors introduced by the nonlinear relation between forces and displacements in the elastomer [47], [48], which we will address in incoming sections. Additionally, when a torque is applied to the sensor, it causes the magnet to rotate and with it, a change in the magnetic field, leading to erroneous force measurements [47]. Some studies have attempted to measure forces and torques with advanced magnetometers [49]. In our study, we limited the rotations around the X and Y axes (see Figure 3a) by placing the moving platform of the interface, to which the sensor is connected, close to the housing of the interface, physically limiting the rotations. The impact of rotations around the Z axis is mitigated by the design of the sensor, as described in the incoming paragraphs.

The proposed design follows the approach and guidelines established by Wang et al. [47], relying on an MLX90393 three-axis magnetometer (Melexis, Belgium) to measure the changes in magnetic field. The magnetometer chip is interfaced via Serial Protocol Interface (SPI) using a $10\,\mathrm{MHz}$ clock signal in single-measurement mode with a $1.55\,\mathrm{ms}$ reading time. The sensor is configured to provide data on the 16 least significant bits of the 19-bit internal analog-to-digital converter (ADC) along the X and Y axes, providing the highest resolution possible. The resolution is set one bit lower along the Z axis, i.e. bits 1-17 of the ADC, due to the strong magnetic field along that axis.

The magnetic field is generated by a $3.0\mathrm{x}1.0\,\mathrm{mm}$ cylindrical neodymium magnet with N48 remanence (MAGZ-087-P, MagnetPartner, Denmark), equivalent to about $1.4\,\mathrm{T}$. The strong remanence of the magnet helps to improve the Signal-to-noise ratio (SNR) of the sensor [47], while its size facilitates its embedding within the elastomer, minimizing undesired misalignments upon deformation. A large air gap between the magnet and the magnetometer increases the displacement of the magnet upon deformation of the elastomer, ultimately increasing the sensitivity of the sensor [47]. Our design features a $3.5\,\mathrm{mm}$ air gap, which is the maximum distance allowing for full enclosure of the magnet in the elastomer.

The design of the elastomer largely conditions the sensitivity and full-scale values of the sensor. Ideally, those values should at least satisfy the requirements defined in Section II-A. Our elastomer design is based on that of Le Signor et al. [49], who measured forces of $5\,\mathrm{N}$ in the normal direction, and $1\,\mathrm{N}$ in the shear direction using a cylindrical elastomer of $6\,\mathrm{mm}$ in diameter by $4\,\mathrm{mm}$ in height. The cylindrical shape contributes to axis-symmetric deformations under shear forces, which can improve the efficacy of the calibration. Additionally, it increases the robustness against rotations around the Z axis while helping to reduce the rotations of the magnet around the other axes upon application of shear forces [49]. To accommodate the increased range of forces, we used DragonSkin 30 (Smooth-On, United States), a silicone with A30 shore hardness, providing twice as much stiffness [52] as that from Le Signor et al. [49]. The height is increased to $4.5\,\mathrm{mm}$ to achieve the aforementioned magnet air gap, and the diameter to $11\,\mathrm{mm}$ to maximize the measurement ranges within the available space in the interface. Such an increase in stiffness and volume was estimated to increase the full-scale ranges to the desired ones.

The sensor was manufactured by mold-casting the elastomer body with an aperture for embedding the magnet. The aperture is sealed later on using a dedicated adhesive (Silpoxy, Smooth-On, United States) [47]. Finally, the elastomer

was attached to the platform on the flat surface closest to the magnet, and the connector for the custom board with the magnetometer on the other. Cyanoacrylate (CA) adhesive (SUPERGLUE, Loctite, United States) was used for this purpose. While the cured CA adhesive increases the overall stiffness of the sensor, potentially impacting the sensitivity, other adhesives were found to fail under the desired forces. Still, a grooved pattern was designed on both surfaces of the elastomer to maximize the strength of the binding provided by the CA adhesive. Figure 3a shows a complete unit of the elastomer with the embedded magnet.

With the manufactured elastomer attached to the magnetometer, force measurements with the sensor can be carried out. To do so, the magnetic readings are converted to milliteslas and zeroed by a constant bias. Because the relation between forces and deformations is largely non-linear and a strong cross-talk between axes occurs, a polynomial expansion of the magnetic field readings is then computed. To perform the conversion from the preprocessed and expanded readings to force data, a mapping function is applied. Both the aforementioned bias and the mapping are learned from a dataset of applied forces and associated magnetic field data during a calibration process. Different approaches were compared for the joint transformation composed of the polynomial expansion and the mapping function, as described in the incoming sections.

3) Electronics: To measure the displacements of the actuators, magnetic rotary encoders (Magnetic Encoder Pair Kit for Micro Metal Gearmotors, Pololu, United States) were mounted in the rear shaft of the brushed DC motors. Considering the reductions at the gearbox and leadscrew, the encoder provides a theoretical resolution of $8.3\,\mu\mathrm{m}$, ultimately degraded by the backslash in the mechanical components. Nonetheless, this approach was found to provide a sufficiently accurate position of the platform for the control purposes described in the incoming section. When sampled at high frequencies, the limited resolution of the encoders led to small oscillations in the readings at constant speed. To obtain a stable signal, a low-pass filter with a $10\,\mathrm{Hz}$ cut-off frequency was applied in real-time to the readings.

Each motor is controlled using a DRV8876 brushed DC motor driver (Texas Instruments, United States) using differential pulse-width modulation (PWM) in slow-decay mode. This driver was selected due to its high current support, active current limiting, and current sensing capabilities. The current measurements provided by the driver, when used in combination with the force sensor, can be used to detect a malfunctioning or jammed component in the system. A $6\,\mathrm{V}$, $2.7\,\mathrm{A}$ step-down voltage regulator (D36V28F6, Pololu, United States) is also employed to extend the range of supply voltages that can be provided to the interface. The use of this regulator prevents small voltage drops in the power supplies due to the high motor currents and facilitates the integration of the interface in future projects by supporting a wider range of input voltages.

Finally, an ESP32 Devkit-V1 microcontroller (Espressif, China) is used to integrate and control all the components. A custom-made printed circuit board was designed to host the drivers, regulator, and microcontroller, as well as the connectors to the sensors and actuators of the interface. Such a dedicated electronic setup increases the robustness of the electronic connections and eases the integration into the hand robot.

4) Controller design: The closed-loop control is achieved by reading the data from the sensors and sending the corresponding control action to the motor drivers. The ESP32 microcontroller is programmed using FreeRTOS, an open-source Real-Time Operating System (RTOS) that allows for predictable and deterministic behavior. The RTOS is used to run the control and the communication tasks separately, ensuring the frequency stability of the control loop. The $1.55\,\mathrm{ms}$ reading time of the force sensor, together with the discretized update period of FreeRTOS to $1\,\mathrm{ms}$ steps, limited the control loop frequency to $500\,\mathrm{Hz}$ to ensure new data from the force sensor is available on every update.

Two control schemes are implemented in the interface. A position control scheme is used to reposition the platform to the center of the ROM when the mechanism calibrates, or large slips with the fingers occur. A proportional (P) controller with gain $k_p = 500$ was used, as it achieved a stable response and very low steady-state error, which were considered sufficient criteria for this task. Control actions with an absolute value in the range 0.1–50 were mapped to 10–100% of the duty cycle, with actions of smaller magnitude, rounded down to 0. The sign of the control action determined which of the two PWM signals commanded to the motor was modified. Such an approach was taken to ensure that the system would overcome the friction in the transmission for a wide range of control actions. Otherwise, low control actions would cause small currents to continuously flow through the stalled motor, potentially damaging it.

A similar voltage-driven approach is adopted for the force control scheme, thanks to the mechanical characteristics of the sensor and the fingerpads. A proportional-integral-derivative (PID) controller was used to achieve a fast transient response (proportional part), accurate steady-state forces (integral part), and minimal overshoots that may lead to an overestimation of the forces by the user (derivative part). The controller gains were manually tuned for each axis until no overshoot nor steady-state error was measured by the magnetic-based force sensor upon a step signal of 1, 2, or $3\,\mathrm{N}$. The resulting gains were: $k_p = 110$, $k_i = 30$, and $k_d = 3$ for the horizontal axis; and $k_p = 200$, $k_i = 100$, and $k_d = 6$ for the vertical axis. The same mapping as for the position control was applied to the control action.

To prevent the actuators from aggressively reaching the ends of the ROMs upon a commanded force, the lateral force rendering is only activated when a normal force acting against the platform is detected. Finally, since slip may occur between the fingers and the platform, control actions moving the system closer than $0.25\,\mathrm{mm}$ to the ends of the ROM are ignored.

C. Experimental evaluation

To evaluate the performance of the system, we first calibrated the magnetic-based force sensor and evaluated the

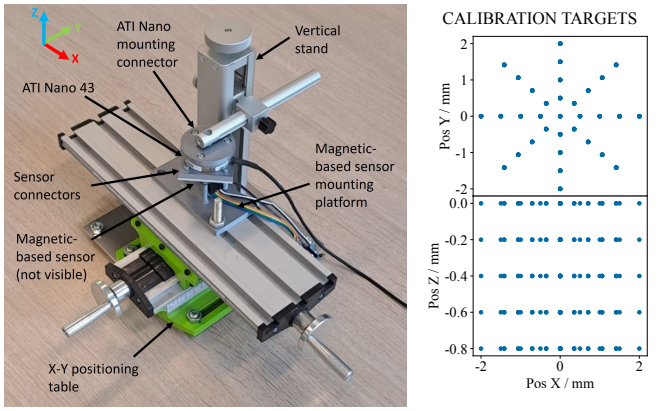

(a) (b)

Fig. 4. (a) Experimental setup used to perform the measurements of the forces applied to the sensor during calibration and characterization and exerted by the interface during its validation. The positioning stage consists of a two-axis positioning table to which the measured system is attached (in the picture, the standalone sensor) and a single-axis vertical stage to which the reference F/T sensor is connected. The sensors are connected through a set of screws linking the 3D-printed connectors attached to each of them. (b) Distribution of the deformations applied to the magnetic-based sensor to collect the data for the calibration of the sensor. The distribution is shown across the X-Y plane (top) and the X-Z plane (bottom).

performance of different mappings. Then, additional tests on the characterization of the sensor were conducted. All these measurements were performed on a standalone unit of the sensor built on a commercial evaluation board (EVB90393, Melexis, Belgium). Doing so allowed us to evaluate the sensor performance in isolation and to obtain results comparable to the literature. Finally, a second unit of the sensor was manufactured, mounted, and calibrated within the tactile interface, whose force-controlled response was evaluated.

1) Experimental setup: All of the measurements and evaluations were conducted with the same setup. To measure the forces applied to the sensor and, eventually, exerted by the tactile interface, an ATI Nano 43 force-torque (F/T) sensor (ATI Industrial Automation, United States) was used.

A three-axis positioning stage was employed to align the reference sensor with the measured system and to apply controlled deformations to the magnetic-based force sensor. The stage consisted of a two-axis positioning table (HBM Machines, The Netherlands) connected through a custom mounting plate to a Dino-Lite RK-10 stand (Dino-Lite Europe, The Netherlands), depicted in Figure 4a. The system being measured was mounted on the positioning table, while the reference F/T sensor was mounted on the stand, allowing relative displacements between the two.

For the measurements carried out in the standalone sensor, a connector was fixed with screws to the reference F/T sensor. On the side of the magnetic-based sensor, a connecting platform was glued using CA adhesive to the top face of the elastomer. The two connecting parts could then be linked using screws. For the measurements carried out with the interface, a modified connector was mounted to the F/T sensor. This connector featured several pins that fit into pre-made holes in the actuated platform, providing a tight link between the two.

To collect the data, the F/T sensor was sampled with a data acquisition card (USB-6351, National Instruments, United States). The information from the tactile interface was sent to the computer through the USB port of the ESP32 microcontroller. The management of the communication and the collection of data was performed in Python. Both systems were simultaneously sampled at the same frequency on separate threads, ensuring the synchronicity of the collected data.

2) Sensor calibration: For the magnetic-based sensor to measure forces, it is necessary to determine the mapping from magnetic field readings to forces [47]. To do so, a dataset was collected by applying deformations to the sensor and recording paired samples of magnetic field and applied force data. The deformations were applied in a controlled way using the positioning stage with the two sensors connected.

Samples were collected from different displacements uniformly distributed over the cylindrical coordinate frame of the sensor (see Figure 4b). The selected ranges were defined to cover the desired maximum force in the radial direction. Forces in the vertical (Z) direction were limited to the 18 N measurement range of the reference F/T sensor. A total of 165 targets were collected by taking 0.2 mm steps in the vertical direction up to 0.8 mm depth, 0.5 mm steps in the radial direction up to 2 mm, and 45° steps in the angular direction. To evaluate the performance of the mapping on unseen data, data from 45 additional randomly generated targets were collected and stored in a separate data file. Data was collected at 100 Hz from both sensors for 1 s at each target location, yielding a total of 100 data points per target displacement.

The collected dataset was then used to learn the transformation from magnetic field data to forces. To do so, we compared combinations of polynomial expansions from order one to four with three different mapping functions, yielding a total of 12 transformations from magnetic field to forces. The three selected mappings were: i) a standard linear regression, ii) a linear regression with parameter optimization via stochastic gradient descent with a Huber loss function and L2 regularization, and iii) a neural network (NN) using Adam optimizer and mean squared error (MSE) loss function. For the training of the NN, 23 out of the 165 calibration samples were used for the validation set, and the rest were used for the training.

The transformations were compared with each other in terms of the L2 norm of the mean absolute errors (MAE) per axis between the F/T sensor and the magnetic-based sensor, both on the calibration and the evaluation datasets. The reported value for the MAE of the NN during training was computed as the average of the MAE during training and validation, weighted by the number of samples of each set, e.g. $(23/165)\text{MAE}_{\text{val}} + (142/165)\text{MAE}_{\text{train}}$. Based on these metrics, a combination of polynomial expansion and mapping function was selected and used for computing the measured forces by the magnetic-based sensor in all subsequent tests.

3) Evaluation under dynamic loading: Due to the dynamic nature of the tasks in which the sensor will be used, we evaluated the performance of the sensor under continuously varying forces. To do so, thirty seconds of paired magnetic field data and F/T sensor readings were collected at 100 Hz.

During that time, different forces were applied along each axis at random using the positioning stage. For the magnetic-based sensor, magnetic field data was collected and mapped offline into forces using the transformation selected during the calibration. The performance was measured as the MAE between the force values from the magnetic-based force sensor and those of the reference F/T sensor along each axis.

4) Magnetic-based force sensor characterization: As mentioned in previous sections, the use of viscoelastic material in the sensor, like silicone, introduces some errors in the measurements. When a deformation is applied to a viscoelastic material, a rearrangement of the molecules takes place to accommodate the deformation [53]. In doing so, friction and back-stress arise at a molecular level, resulting in larger forces required to apply the deformation than to remove it [54]. Such a response is denoted as hysteresis and can cause a similar behavior in measured versus applied force during a loading and unloading cycle [47]. Similarly, the rearrangement of molecules in the material upon deformation, also denoted as creep, results in reduced force required to induce the same deformation over time [53]. As a result, the sensor may overestimate the magnitude of a sustained force [47]. It was therefore important to quantify these effects to get a better estimate of the performance and limitations of the proposed sensor.

Furthermore, the sensor is known to be sensitive to rotations of the magnet. Despite the measures taken to minimize this effect through the design of the sensor and the interface, we investigated the impact of rotations around all three axes. By doing so, we aimed to achieve a complete characterization of the sensor and its limitations. For all tests, data was collected and processed in the same way as for the evaluation under dynamic loading.

To evaluate the hysteric error introduced by the silicone, a loading-unloading cycle was applied through an indentation of $0.5\,\mathrm{mm}$ in the Z direction, and of $1.25\,\mathrm{mm}$ in the X and Y directions. During the X and Y measurements, a $0.2\,\mathrm{mm}$ indentation in the Z direction was applied to recreate the working conditions in which the sensor will be used. The difference in the readings from the magnetic-based sensor during loading and unloading was then computed at half of the applied force (as measured by the F/T sensor). The hysteresis was finally calculated as the fraction between that difference and the magnitude of the applied force, in percentage.

To evaluate the influence of viscoelastic creep, the same indentations as in the hysteresis test were applied and sustained for a total of $30\,\mathrm{s}$. The difference between the readouts of the magnetic-based sensor and the F/T sensor was computed after $5\,\mathrm{s}$, once the applied force had approximately stabilized, and after $30\,\mathrm{s}$ of the force onset. The creep was then computed as the magnitude of the increase between those two measures.

To assess how rotations along each axis affect the measurements, we incorporated modified connectors into the reference F/T sensor. Each connector aligned with the magnetic-based sensor at a $15°$ rotation around each of the three axes. This value was considered the maximum rotation induced during normal usage of the interface around the Z axis, the only unconstrained in the design. Data was collected during $20\,\mathrm{s}$ starting with the sensor in the rest state. Then, for the X and Y rotations, the positioning stage was lowered to make contact with the magnetic-based sensor. In doing so, the tilted surface of the modified F/T sensor connector induced the desired rotation on the magnetic-based sensor. For the Z rotation, the connector of the magnetic sensor was manually aligned with that of the F/T sensor and then held in place using a set of pins passing through both connectors. The impact of the rotation was measured as the variation in the measurement error at the start and end of the collection, disregarding intermediate data during alignment. The variations are computed along each axis, as well as the variation in three-dimensional measurement error, computed as the difference in the L2 norm of the errors at the beginning and the end of the collection.

5) Force control validation: A second unit of the force sensor was manufactured and mounted within the tactile interface. The sensor was calibrated inside the interface as described in Section II-C2. The transformation from magnetic readings to forces was implemented on the microcontroller using the weights obtained during the calibration. This way, together with the PID controller described in Section II-B4, the desired closed-loop force control architecture was achieved. Due to the high-frequency noise observed in the standalone sensor evaluation and characterization, a low-pass filter with a $10\,\mathrm{Hz}$ cut-off frequency was used. The filter was implemented using Euler-backward discretization in the microcontroller and applied in real-time.

To validate the force-controlled interface, we first performed a step response test to evaluate its temporal and steady-state response. A bandwidth test was then conducted to determine the usable frequency range of the device. In both tests, data was collected at $500\,\mathrm{Hz}$, matching the control frequency of the tactile interface, and both from the interface and the reference F/T sensor. A normal force of $2\,\mathrm{N}$ was applied at all times.

For the step response test, we recorded the response of the system during 10 steps of 1, 2, and $3\,\mathrm{N}$ of amplitude (30 steps in total) along the positive horizontal, vertical, and $45°$ directions. Each step lasted 2 seconds and was preceded and followed by 1 second at zero force. The amplitudes and directions tested allowed us to investigate the 2-DoF rendering capabilities of the interface in the ranges of forces where tactile information dominates force perception [33], [36]. The rise time was calculated as the time required to rise from 10% to 90% of the steady-state value of the corresponding signal, while the steady-state error was measured as the error after $1.8\,\mathrm{s}$ of commanding the step. The metrics were computed for each step and averaged across the 30 steps per direction, both for the magnetic-based sensor and the F/T sensor data.

For the bandwidth test, we commanded an exponential chirp signal that swept from 1 to $100\,\mathrm{Hz}$ at a constant amplitude of $1\,\mathrm{N}$ ($2\,\mathrm{N}$ peak-to-peak) for 10 seconds. From it, we computed the Fast Fourier Transform to obtain the magnitude of each frequency component for the commanded signal and the response of the system. Finally, the value of the gain was obtained as the ratio between those two magnitudes, yielding the final Bode plots of the frequency response. We performed this calculation using both the readings from the magnetic-based sensor and the reference F/T sensor.

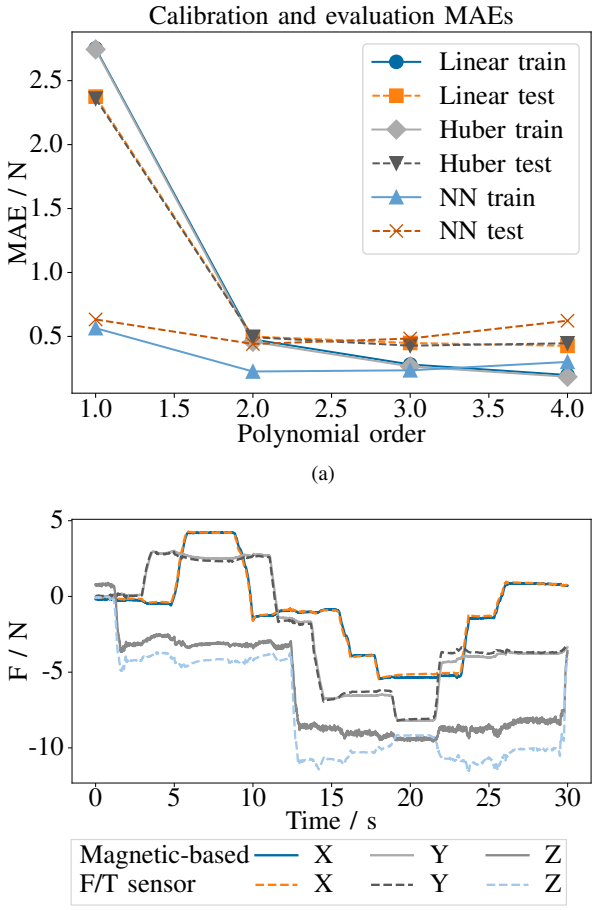

Fig. 5. (a) L2 norm of the MAE between the sensor predictions and F/T sensor readings during training and evaluation for different models as a function of the degree of the polynomial expansion of the magnetic field data. (b) Results from the continuous evaluation test. The continuous lines display the forces measured by the magnetic-based sensor and the dashed lines by the reference F/T sensor.

III. Results

A. Sensor calibration

To calibrate the sensor, we collected samples of magnetic field data and associated force data under different deformations of the elastomer. The 2 mm shear displacements caused forces of up to 8 N along the X and Y axes, while the 0.8 mm indentation yielded normal forces of up to 16 N along the Z axis. A total of 13 out of the 165 samples were discarded due to an overflow of the 16-bit readings from the sensor during large displacement in the +X/+Y direction. One additional data point from a sample was also discarded due to a corrupted reading from the data acquisition system. From the additional evaluation dataset, 3 out of the 45 samples were discarded due to overflow of the readings in the +X axis.

Figure 5a shows the MAE (computed as the L2 norm of the MAE along the three axes) on the calibration and evaluation data for the different combinations of mapping functions and polynomial expansion orders. The lowest calibration error was found for the Huber regression, yielding 0.184 N, while the lowest evaluation error corresponded to the Linear regression, with 0.426 N, in both cases using an order 4 polynomial expansion. However, due to the similar performance of the models beyond an order 3 polynomial expansion, we opted for a simpler model, less prone to overfitting, and more computationally efficient. Therefore, the Huber regression on an order 3 polynomial expansion was selected for the transformation of the data collected in subsequent tests.

Further inspection of the results from the Huber regression on the order 3 polynomial expansion yielded an MAE and standard deviation (SD) of 0.068 ± 0.102 N in the X-axis, 0.056 ± 0.053 N in the Y-axis, and 0.250 ± 0.260 N in the Z-axis during training. On the evaluation set, values of 0.09 ± 0.072 N in the X-axis, 0.152 ± 0.100 N in the Y-axis, and 0.39 ± 0.28 N in the Z-axis were observed. Visual inspection of the results showed that the magnitude of the errors was constant throughout the ranges of forces applied. No overall bias across the measured ranges was observed either.

B. Evaluation under dynamic loading

The performance of the sensor was evaluated during dynamic force profiles. Figure 5b shows the forces applied to the sensor, measured by both the magnetic-based sensor and the reference F/T sensor. The forces from the magnetic-based sensor were computed offline using the model selected in the previous section. The test yielded MAEs and SDs of 0.108 ± 0.094 N in the X-axis, 0.181 ± 0.156 N in the Y-axis, and 1.355 ± 0.627 N in the Z-axis.

C. Force sensor characterization

The results of the characterization of the hysteresis and viscoelastic creep are shown in Figure 6.

With regards to the hysteresis tests, in the X axis, a difference of 0.617 N was observed at the central value of the range of forces applied, corresponding to a hysteresis of 11.571%. In the Y axis, a similar difference of 0.691 N was observed, equivalent to a hysteresis of 12.395%. Along the Z axis, a large offset was observed in the magnetic-based sensor measurements. An initial offset of 1.168 N was observed under no-load conditions at the beginning of the collection, which increased to 2.717 N under the 12.806 N of maximum load applied during the test. When looking at the central values during the loading and unloading cycle, a difference of 1.823 N was observed, corresponding to a 13.579% hysteresis.

For the viscoelastic creep, along the X axis, the error increased from 0.043 N to 0.133 N, 5 s and 30 s after the application of the force, respectively, resulting in a creep of 0.090 N. Along the Y axis, the error increased from 0.085 N to 0.143 N, resulting in a creep of 0.058 N. On the Z axis, an initial error of 0.993 N was observed in the magnetic-based sensor under no-load conditions. After the application of the force, the error increased to 1.842 N and eventually to 1.330 N, indicating a creep of 0.508 N.

Finally, Table I shows the variations in the measurement error along each axis by the effect of rotating the surface of the sensor around each of the three axes. The last column displays the variation in the three-dimensional measurement error after the rotation.

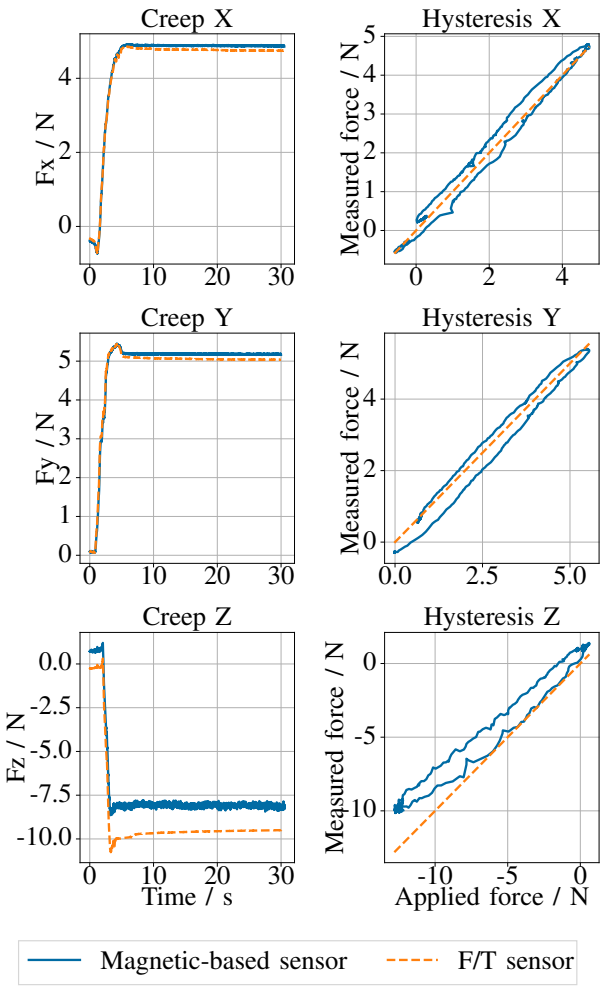

Fig. 6. Viscoelastic creep and hysteresis response of the sensor along the X, Y, and Z axes.

TABLE I
VARIATIONS IN ERROR INDUCED BY PLATFORM ROTATIONS

Rotated axis	**ΔFx** / N	**ΔFy** / N	**ΔFz** / N	‖**ΔF**‖ / N
X	-0.071	1.388	4.926	5.113
Y	1.327	0.192	6.538	6.647
Z	0.201	-0.137	0.843	0.839

D. Force control validation

To evaluate the performance of the force-controlled interface, the new unit of the sensor mounted in the device was first calibrated. Then, the performance of the system was evaluated in terms of step response and frequency response.

1) Calibration of mounted magnetic-based force sensor: The calibration and evaluation process was repeated for the sensor mounted inside the tactile interface. The 2 mm shear deformations induced maximum forces of approximately ±6 N along the X and the Y axis. The 0.8 mm normal indentation yielded forces of up to 6 N. None of the samples showed overflow from the ADC of the magnetometer.

Following the results of the standalone sensor, the Huber regression model with the polynomial expansion of order 3 was trained on the calibration data and evaluated on the additional dataset. The results from the calibration yielded an MAE and SD of 0.069±0.081 N in the X axis, 0.075±0.067 N in the Y axis, and 0.184±0.151 N in the Z axis during training. On the evaluation set, values of 0.214±0.109 N in the X axis, 0.095 ± 0.105 N in the Y axis, and 1.451 ± 0.337 N in the Z axis were observed.

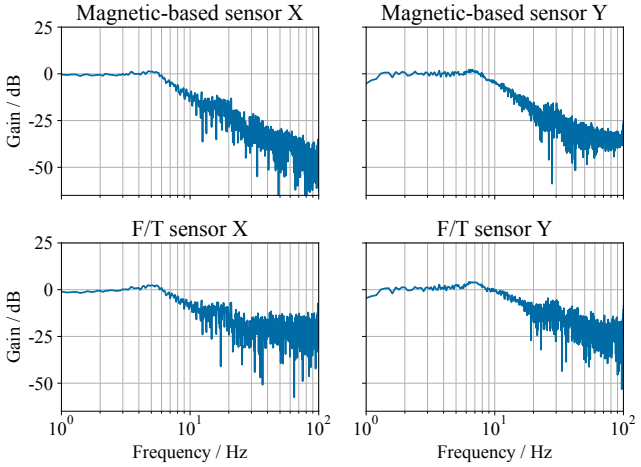

Fig. 7. Bode plots generated from the collected data for the evaluation of the frequency response. The plots depict the gain of the response of the system with respect to a commanded chirp signal of constant amplitude. The top row corresponds to the response as measured by the magnetic-based force sensor, while the bottom row shows the response of the system as measured by the reference F/T sensor.

2) Step response: We commanded a series of step signals to the interface along different axes. The rise time, as measured by the magnetic-based sensor, was 0.063 s, 0.065 s, and 0.071 s along the X, Y, and diagonal directions. When measured by the F/T sensor, the value decreased to 0.026 s, 0.018 s, and 0.050 s along the X, Y, and diagonal directions.

Regarding the steady-state error of the magnetic-based sensor, an average error of 0.009 N, 0.028 N, and 0.037 N was observed along the X, Y, and diagonal directions. Considering the readings from the F/T sensor, the steady state error increased to 0.279 N, 0.441 N, and 0.362 N along the X, Y, and diagonal directions.

Finally, while no overshoot was observed in the magnetic-field sensor, the F/T sensor indicated an overshoot of 25.541% with respect to its steady-state value along the X axis, 17.306% along the Y axis, and 15.556% in the diagonal direction.

3) Frequency response: We commanded a chirp signal of constant amplitude along each axis of the system. The Bode plots in Figure 7 represent the gain of the system response with respect to the commanded signal as measured by the magnetic-based sensor and the F/T sensor. A gain-crossover frequency was observed around 5 Hz and 7 Hz for the X and Y axes, respectively, where a small resonance can be observed. The response of the magnetic-based sensor, being processed in the microcontroller by the low-pass filter, presented greater attenuation than that of the F/T sensor.

IV. Discussion

Neuroscience studies have suggested that the provision of somatosensory information can improve the motor recovery of stroke patients [7]. Despite the importance of tactile information for motor control [17], [19], its inclusion in robotic neurorehabilitation systems remains largely unexplored. This study presented a novel tactile interface to extend the haptic rendering capabilities of an existing hand rehabilitation robot [1]. The interface applies force-controlled skin stretch stimulation to the fingerpads, relying on a custom magnetic-based force sensor to measure the rendered forces. We investigated the force-sensing accuracy of the proposed sensor and characterized the impact of hysteresis, viscoelastic creep, and platform/magnet rotations on the measured forces. A second sensing unit was mounted and calibrated on the tactile interface. The performance of the resulting force-controlled system was evaluated in terms of step response and frequency response.

A. The proposed interface preserves key features of the robot while providing versatile multi-finger rendering

Aiming for seamless integration into the hand rehabilitation robot, the proposed design of the interface featured minimal changes in size with respect to the original finger end-effector of the robot [1]. Thus, the interface only extends the size of the end-effector along one dimension, as indicated in Figure 2b, to accommodate the 0–165° ROM for the finger flexion. While this extension in size reduced the thumb flexion ROM by approximately 10°, and the circumduction ROM by 15°, this could be mitigated in future versions through a more compact and optimized design. Nevertheless, the proposed design successfully preserves the ROM of the finger flexion and the setup of the hand in the robot in a closed position.

When looking into the rendering capabilities of the interface, the 2-DoF actuated platform successfully covers the tangential plane of the fingerpads. As previously mentioned, the mechanism features a range of motion of $\pm 4.5\,\mathrm{mm}$, limited by the deformations of the magnetic-based sensor to $\pm 3\,\mathrm{mm}$. While increasing the stiffness of the elastomer can extend the ROM, adjustments in the actuator can have the greatest impact in this regard. Employing more compact actuators with a leadscrew directly mounted to the gearbox or alternative transmission mechanisms can help increase the ROM to the $\pm 5\,\mathrm{mm}$ requirement. Still, the current ROM suffices for rendering forces up to $3\,\mathrm{N}$, where tactile information is more critical for the perception of force and weight [33], [36], [45].

While the ROMs limit the maximum forces rendered by the interface, preliminary tests indicated that up to $5\,\mathrm{N}$ could be achieved by the interface, meeting the corresponding requirement of this study. However, achieving those levels of actuation while withstanding the grasping forces rendered by the robot, which can be as large as $30\,\mathrm{N}$ [1], remains an open challenge. While the proposed design aimed to do so by allowing contact between the moving platform and the housing of the interface, this leads to friction forces that can degrade the rendering accuracy and still limit the maximum actuation. Future efforts should be directed toward maintaining a constant air gap between the platform and the housing while enhancing the design of the mechanism. Higher-performance components, though increasing the cost of the interface, can largely contribute to this regard, as demonstrated by previous studies relying on similar actuation mechanisms [46].

Finally, many previous skin stretch devices were limited to single-finger stimulation [23], [28], [29]. Those acting upon multiple fingers are typically bulky and constrain the hand position to a pinch grasp, only stimulating the thumb and index fingers [33], [34]. The proposed device achieves multi-finger stimulation in a compact size, allowing the preservation of key features of the hand rehabilitation robot. Additionally, the integration of the interface in the robot allows the possibility to render three-dimensional interaction forces, thanks to the 2-DoF actuation of the interface, covering the ranges of forces where tactile information is most critical.

B. Our sensor achieves large measurement ranges with a small size and an accuracy comparable to the state-of-the-art

The collected calibration data for the sensor covered a range of $\pm 8\,\mathrm{N}$ in the X and Y axes, and $16\,\mathrm{N}$ in the Z axis. These ranges are the largest recorded for a sensor of such a small size, in particular for the shear forces, typically ranging $\pm 1\,\mathrm{N}$ [47], [49], [55]. The only other study achieving similar measurement ranges was 10 times as large as the one presented in this study [56]. The large measurement-range-to-size ratio of our sensor was partly thanks to the use of a stiffer elastomer, but also due to the application of forces to the sensor through a rigidly connected platform. Doing so allowed the application of shear forces that would have otherwise caused slippage with the surface of the sensor [47].

When comparing the calibration data from the standalone and interface-mounted sensors, notable differences can be appreciated. Even though the same displacements of the stage were used, the measurement ranges of the sensor unit mounted in the interface were smaller than those of the standalone sensor. This reduction can be partly attributed to variations during manufacturing. For example, different amounts of the CA adhesive used for attaching the elastomer with the platform and connector, once cured, could have affected the overall stiffness of the elastomer differently. Another factor contributing to this phenomenon is the compliance of the mechanism under the applied forces. As a result, the sensor was not deformed by the same magnitude as the positioning stage was displaced, ultimately resulting in smaller forces applied for the same displacements of the stage. This effect was most noticeable along the Z axis, in which the compliance of the mechanism combined with partial contact between the platform and the housing of the device resulted in very small deformations. This result highlights the need for in-situ calibration of the sensor, in addition to the unit-by-unit calibration due to variations during hand-made manufacturing [57].

During the comparison of transformations from magnetic data to force data, it was observed that all models performed roughly equivalently on polynomial expansions of order 3 and 4. The slight improvement with the order 4 expansion only on the training data indicated a degradation in the generalization

of the model and so, the order 3 expansion was selected. Coinciding with the results of Tomo et al. [48], the linear regressors performed better than the neural network. This is also supported by previous literature, in which more complex network-based calibrations achieve accuracies of 2% of the full-scale value [55], while studies relying on polynomial expansion and linear regressors achieve up to 0.07% [47], [49].

When inspecting the performance of the selected transformation, we obtained MAE of up to 250 mN along the X and Y axes, and up to 770 mN along the Z axis. Considering the measurement ranges of our sensor, this corresponds to a resolution of 1.56% of the full-scale range in X and Y, and 4.813% in Z. Previous literature has presented values ranging between 0.71–11.7 mN, or 0.07–2.2% of the full-scale [47], [49], [55]. The resolution of our sensor leans toward the lower resolution values in the literature, which can be attributed to the data used for the calibration. Due to the use of a manual positioning stage, the collection of data proved very time-consuming, limiting the calibration dataset to 165 distinct samples spanning over the three sensing axes. Previous studies used automated positioning stages to collect up to 4800 samples over two of the measurement axes [47], or 13000 samples collected over the three axes [49]. Such an extensive sampling of the forces applied to the system could explain the increased resolution reported in those studies.

The results from the dynamic load test yielded similar errors along the X and Y axes as in the static calibration and evaluation. Along the Z axis, a larger error offset of varying magnitude was observed, which will be addressed in incoming paragraphs. Overall, the results indicate that the calibration performed on the sensor generalizes to continuously varying data, aligning with previous literature [47], [49].

When comparing these results with the original requirements of the system, the full-scale range of the sensor covers the desired ranges of actuation of the interface. However, further work needs to be done to lower the measurement error to meet the 50–100 mN requirement originally set for the interface. This could be achieved by introducing temperature compensation both for the magnetometer readouts [48] and the changes induced by the expansion/compression of the elastomer [49]. Previous literature has also achieved high resolutions by using multiple magnetometers [56] or an integrated circuit with multiple magnetic field-sensing units [49]. Finally, the calibration procedure needs to be improved by increasing the number of samples and the way they are collected to reduce the aforementioned offsets in the Z axis, which also impacts the accuracy of the remaining axes.

In summary, the proposed sensor achieves accuracies within the values reported in the literature, as well as the highest measured-force-to-size ratio for this kind of sensor. Future works should focus on further improving the accuracy to meet the targetted value, by adopting some of the calibration and compensation strategies reported in the literature.

C. The accuracy of the sensor is largely impacted by large deformations and rotations

The results of the hysteresis tests yielded errors around 11–13% along all the axes. In previous literature, only a value of 3.4% is reported in one study [47], with another reporting no hysteresis with respect to the applied force [55], both of them in the normal direction (Z axis). One possible explanation for the increased magnitude of the hysteresis is the larger deformation applied to the sensor, in particular along the X and Y axes. Another possible explanation is that the dataset that we used for calibration only contained samples collected during static, step-wise loading. Gathering an increased number of samples both during loading and unloading or during dynamic force application may help reduce these errors.

The measurement of viscoelastic creep in the shear direction is a novelty for this type of sensor. During the test, the measured force by the sensor was observed to change over the 25 s in which the force was sustained. The change was about 2% of the applied force in the X and Y axes and 5% in the Z axis. Wang et al. [47] had previously measured a creep of about 3% in the normal direction, which aligns well with our results, despite the difference in materials (shore 00-30 hardness versus the shore A30 used in this study). Additionally, the results of our test indicate that creep effects are less prominent in the shear direction than in the normal direction.

Finally, this study also provides a quantitative measurement of the impact of rotations on the measured forces. As expected, the rotations around the X and Y axes caused increases in the measurement error of about 1.4 N on the Y and X axes, respectively. In both cases, the measurements in the Z axis drifted by about 6 N. When a rotation is applied around an axis, the changes perceived by the magnetometer are equivalent to a combined shear and normal deformation. This result highlights the importance of constraining such rotations to achieve accurate force readings. An alternative approach would rely on the use of more sensing units for simultaneous measurement of forces and torques [49], [56]. When looking at the impact of rotations around the Z axis, slight variations in the measurements were observed. This was attributed to imprecisions in the placement of the magnet inside the elastomer which led to deviations from the ideal axis-symmetric design of the sensor. While the errors around the Z axis were much smaller than around the X or Y axes, they were of a similar magnitude to the sensor accuracy. The effect of the rotation around Z can be addressed in a similar way to the other axes. However, a more careful alignment of the magnet within the elastomer can also contribute to mitigating this effect [57].

One major issue was the presence of a large offset along the Z axis of the sensor, both for the characterization data of the standalone sensor and the evaluation data of the mounted sensor. By inspecting the raw data from the calibration dataset of the standalone sensor, it was observed that at zero shear force, the 0–16 N normal forces caused the magnetic field intensity to change by approximately 2 mT. When looking at the no-load magnetic field readings from the characterization datasets, the magnetic field measurements along the Z axis were found to be 0.25–0.3 mT lower than in the calibration dataset. This difference increased when comparing the data under similar levels of applied pressure in the normal (Z) direction. One possible explanation for the generalized change in magnetic

field measurements is a long-lasting or permanent deformation of the elastomer after the large deformations applied to it. As a result, the magnet lies further from the magnetometer, causing a decrease in the magnitude of the magnetic field, and an overestimation of the applied forces. It should be noted that considering the design and observed values, the described change in magnet position causing this offset would be of less than $100\,\mu\mathrm{m}$. Another possible explanation for these changes in the readings is the effect of temperature. In an effort to increase the measurement rate of the sensor, temperature compensation was not implemented in the magnetometer readings. Some studies have reported variations in the readouts of the magnetometer as a result of temperature variations [48], as well as in the force measurements due to the expansion of the elastomer [49]. Finally, the impact of these variations was found to be much larger in the sensor mounted in the interface, where the applied normal forces during calibration spanned a range of only $0.7\,\mathrm{mT}$.

To address the aforementioned issues, in addition to implementing temperature compensation strategies [48], [49], careful selection of the elastomer should be performed. The choice of a stiffer material or shape of the elastomer can contribute to a reduction of the hysteresis, viscoelastic creep, and the large offset observed in the Z axis. When considering the wider picture of the tactile interface, force sensing is only required along the actuated axes. Therefore, a planar sensor design, constraining both the Z axis and the rotations could address several of the discussed issues. To measure normal pressure, if needed, a separate force-sensitive resistor or other off-the-shelf and inexpensive single-axis compression sensors could be used. Such an approach would have the added benefit of preventing errors along the Z axis to influence measurements in the X and Y axes (due to the polynomial expansion computed on the magnetic readings). Finally, it would drastically reduce the amount of samples required to calibrate the sensor, contributing to an improvement in sensor accuracy.

D. The interface achieves a fast and consistent rendering, with limited accuracy and quality of stimulus

To evaluate the performance of the force-controlled interface, we conducted a step response and a frequency response test. The results of the step response test yielded rise times of 0.02–0.07 s. Larger rise times were observed in the measurements of the magnetic-based sensor than in those of the F/T sensor. Inspection of the raw data indicated that, while the onset of the force occurred simultaneously, the force increased more smoothly in the magnetic-based sensor readings. This response, as well as the larger rise times, are likely caused by the low-pass filter applied to the magnetic-based sensor readings. In any case, these results indicate that the initial objective of 0.35 s rising time is broadly satisfied.

The good temporal response of the interface is further supported by the results of the frequency response tests, which yielded a gain-crossover frequency at 5–7 Hz. While the response as measured by both sensors resulted in similar gain-crossover frequencies, larger attenuation due to the low-pass filter was observed in the magnetic-based sensor data. To completely cover the ranges of forces during object interaction, future versions of the system should aim to increase the effective bandwidth of the actuator to 10 Hz, which is regarded as the maximum frequency of human movement [58]. As previously discussed, studies employing similar actuation methods achieved a bandwidth of 20 Hz, suggesting that improved components and more accurate manufacturing processes can enhance the performance of the system. Nonetheless, the response of the interface is similar to other skin stretch devices [23] and should cover a wide range of motions and interactions.

With regards to the rendering accuracy, the steady-state errors measured by the reference F/T sensor observed during the step response tests are still much larger than the 50–100 mN. Such a large magnitude is attributed to the measurement error in the magnetic-based sensor and the friction between the moving platform and the housing of the interface. The low steady-state errors measured by the magnetic-based sensor and the reduced variation in magnitude of the errors across the range of step amplitudes support this explanation. Future works should focus on improving the accuracy of the sensor and reducing the friction between the moving platform and the housing of the interface, as mentioned in previous paragraphs.

In addition to the aforementioned limitations, three considerations should be taken to improve the stimuli provided by the interface. When looking at the step response data, an overshoot was observed in the reference F/T data which was not observed in the magnetic-based sensor data. In addition to the lower temporal resolution of the proposed sensor, the low-pass filter applied to the magnetic-field readings is also suspected to have contributed to this. Therefore, additional tuning of the filter parameters needs to be performed to fully capture the response of the system and to properly adjust the gains of the controllers to prevent overshoots. Another major point of improvement relates to the grounding of the fingers. The current version of the finger fixation in the robot allows some fingers to move upon displacement of the platform. Increasing the amount of padding and a more physiologically aligned design may contribute to the tactile isolation of the stimulus. Finally, due to the compliance of the magnetic-based sensor and its connection point with the moving platform, we found that movements in the proximodistal direction (horizontal, or X direction) led to a rotation of the platform around the normal axis to the fingerpads (Z direction). This ultimately translated into higher deformation and forces exerted at the index and middle fingers, than at the ring and little fingers. The discussed increase in stiffness of the sensor can help reduce the magnitude of the rotations. Alternatively, the use of a secondary sensor unit, located closer to the ring and little fingers can largely constrain such rotation.

From the perspective of the hand rehabilitation robot [1], the robustness of the force-controlled approach allows for consistent rendering for all hand and finger sizes. An additional benefit of the force control is the increase in transparency of the robot, by compensating for small deviations between the trajectory of the end-effector of the finger flexion mechanism and that of the fingers [1]. However, further work is needed to increase the accuracy of the rendering and guarantee the same

consistency under varying grasping forces. Nevertheless, the force-controlled approach allows us to address the dependence on finger pad stiffness for force rendering [23], [28], [29]. In contrast with previous force-controlled systems [33], [34], the proposed interface achieves a multi-finger and compact design, with a wide range of usable frequencies.

V. Conclusion

Existing robotic neurorehabilitation systems largely neglect the provision of tactile information, a crucial component for motor control when interacting and manipulating objects. This study presented a novel tactile interface relying on force-controlled skin stretch stimulation. The interface was designed to extend the rendering capabilities of an existing hand rehabilitation robot with tactile stimulation, and additional considerations were taken to ensure its adequacy for the rehabilitation domain. To achieve the desired force control scheme, while maintaining a low manufacturing cost, we employed a custom three-axis magnetic-based sensor to measure the rendered forces. While further work is needed to mitigate some sources of errors, the sensor achieved accuracies on the actuated axes of the interface close to the state-of-the-art and the highest measurement-range-to-size ratio for this kind of sensor. As for the interface, several tests were conducted to validate its performance and identify areas of future work. The resulting design introduces the novelty of simultaneous stimulation from the index to the little finger, as well as closed-loop force control in a compact and inexpensive solution. By intentionally designing this interface for its use in the rehabilitation domain, we hope that this study serves as a stepping stone towards the inclusion of tactile rendering in robotic neurorehabilitation systems, and ultimately, an enhanced recovery and quality of life for stroke survivors.

References

[1] R. Rätz, F. Conti, R. M. Müri, and L. Marchal-Crespo, "A Novel Clinical-Driven Design for Robotic Hand Rehabilitation: Combining Sensory Training, Effortless Setup, and Large Range of Motion in a Palmar Device," *Frontiers in Neurorobotics*, vol. 15, p. 748196, Dec. 2021. [Online]. Available: https://www.ncbi.nlm.nih.gov/pmc/articles/PMC8721892/

[2] V. L. Feigin, M. Brainin, B. Norrving, S. Martins, R. L. Sacco, W. Hacke, M. Fisher, J. Pandian, and P. Lindsay, "World Stroke Organization (WSO): Global Stroke Fact Sheet 2022," *International Journal of Stroke*, vol. 17, no. 1, pp. 18–29, Jan. 2022, publisher: SAGE Publications. [Online]. Available: https://doi.org/10.1177/17474930211065917

[3] S.-M. Lai, S. Studenski, P. W. Duncan, and S. Perera, "Persisting Consequences of Stroke Measured by the Stroke Impact Scale," *Stroke*, vol. 33, no. 7, pp. 1840–1844, Jul. 2002, publisher: American Heart Association. [Online]. Available: https://www.ahajournals.org/doi/full/10.1161/01.STR.0000019289.15440.F2

[4] L. Mercier, T. Audet, R. Hébert, A. Rochette, and M.-F. Dubois, "Impact of Motor, Cognitive, and Perceptual Disorders on Ability to Perform Activities of Daily Living After Stroke," *Stroke*, vol. 32, no. 11, pp. 2602–2608, Nov. 2001, publisher: American Heart Association. [Online]. Available: https://www.ahajournals.org/doi/full/10.1161/hs1101.098154

[5] J. Tollár, F. Nagy, B. Csutorás, N. Prontvai, Z. Nagy, K. Török, E. Blényesi, Z. Vajda, D. Farkas, B. E. Tóth, I. Repa, M. Moizs, D. Sipos, A. Kedves, A. Kovács, and T. Hortobágyi, "High Frequency and Intensity Rehabilitation in 641 Subacute Ischemic Stroke Patients," *Archives of Physical Medicine and Rehabilitation*, vol. 102, no. 1, pp. 9–18, Jan. 2021. [Online]. Available: https://www.sciencedirect.com/science/article/pii/S0003999320305281

[6] P. Cunningham, A. J. Turton, F. Van Wijck, and P. Van Vliet, "Task-specific reach-to-grasp training after stroke: development and description of a home-based intervention," *Clinical Rehabilitation*, vol. 30, no. 8, pp. 731–740, Aug. 2016. [Online]. Available: http://journals.sagepub.com/doi/10.1177/0269215515603438

[7] M. L. Turville, L. S. Cahill, T. A. Matyas, J. M. Blennerhassett, and L. M. Carey, "The effectiveness of somatosensory retraining for improving sensory function in the arm following stroke: a systematic review," *Clinical Rehabilitation*, vol. 33, no. 5, pp. 834–846, May 2019, publisher: SAGE Publications Ltd STM. [Online]. Available: https://doi.org/10.1177/0269215519829795

[8] S. Meyer, A. H. Karttunen, V. Thijs, H. Feys, and G. Verheyden, "How Do Somatosensory Deficits in the Arm and Hand Relate to Upper Limb Impairment, Activity, and Participation Problems After Stroke? A Systematic Review," *Physical Therapy*, vol. 94, no. 9, pp. 1220–1231, Sep. 2014. [Online]. Available: https://doi.org/10.2522/ptj.20130271

[9] T. B. Scalha, E. Miyasaki, N. M. F. V. Lima, and G. Borges, "Correlations between motor and sensory functions in upper limb chronic hemiparetics after stroke," *Arquivos de Neuro-Psiquiatria*, vol. 69, pp. 624–629, Aug. 2011, publisher: Academia Brasileira de Neurologia - ABNEURO. [Online]. Available: https://www.scielo.br/j/anp/a/FBmc6NfwhK4BBVJD9W3zN6z/?lang=en

[10] N. Bolognini, C. Russo, and D. J. Edwards, "The sensory side of post-stroke motor rehabilitation," *Restorative Neurology and Neuroscience*, vol. 34, no. 4, pp. 571–586, Jan. 2016, publisher: IOS Press. [Online]. Available: https://content-iospress-com.tudelft.idm.oclc.org/articles/restorative-neurology-and-neuroscience/rnn150606

[11] R. Gassert and V. Dietz, "Rehabilitation robots for the treatment of sensorimotor deficits: a neurophysiological perspective," *Journal of NeuroEngineering and Rehabilitation*, vol. 15, no. 1, p. 46, Jun. 2018. [Online]. Available: https://doi.org/10.1186/s12984-018-0383-x

[12] G. Saposnik, M. Levin, and n. null, "Virtual Reality in Stroke Rehabilitation," *Stroke*, vol. 42, no. 5, pp. 1380–1386, May 2011, publisher: American Heart Association. [Online]. Available: https://www.ahajournals.org/doi/full/10.1161/STROKEAHA.110.605451

[13] K. O. Johnson, "The roles and functions of cutaneous mechanoreceptors," *Current Opinion in Neurobiology*, vol. 11, no. 4, pp. 455–461, Aug. 2001. [Online]. Available: https://www.sciencedirect.com/science/article/pii/S0959438800002348

[14] L. Willemet, K. Kanzari, J. Monnoyer, I. Birznieks, and M. Wiertlewski, "Initial contact shapes the perception of friction," *Proceedings of the National Academy of Sciences*, vol. 118, no. 49, p. e2109109118, Dec. 2021, publisher: Proceedings of the National Academy of Sciences. [Online]. Available: https://www.pnas.org/doi/abs/10.1073/pnas.2109109118

[15] J. Park, B. Son, I. Han, and W. Lee, "Effect of Cutaneous Feedback on the Perception of Virtual Object Weight during Manipulation," *Scientific Reports*, vol. 10, no. 1, p. 1357, Jan. 2020, number: 1 Publisher: Nature Publishing Group. [Online]. Available: https://www.nature.com/articles/s41598-020-58247-5

[16] N. Afzal, E. Stubbs, H. Khamis, A. J. Loutit, S. J. Redmond, R. M. Vickery, M. Wiertlewski, and I. Birznieks, "Submillimeter Lateral Displacement Enables Friction Sensing and Awareness of Surface Slipperiness," *IEEE Transactions on Haptics*, vol. 15, no. 1, pp. 20–25, Jan. 2022, conference Name: IEEE Transactions on Haptics.

[17] R. S. Johansson, "Dynamic Use of Tactile Afferent Signals in Control of Dexterous Manipulation," in *Sensorimotor Control of Movement and Posture*, ser. Advances in Experimental Medicine and Biology, S. C. Gandevia, U. Proske, and D. G. Stuart, Eds. Boston, MA: Springer US, 2002, pp. 397–410. [Online]. Available: https://doi.org/10.1007/978-1-4615-0713-0_45

[18] M. Wiertlewski, S. Endo, A. M. Wing, and V. Hayward, "Slip-induced vibration influences the grip reflex: a pilot study," in *2013 World Haptics Conference (WHC)*, Apr. 2013, pp. 627–632.

[19] J. M. Walker, A. A. Blank, P. A. Shewokis, and M. K. O'Malley, "Tactile Feedback of Object Slip Facilitates Virtual Object Manipulation," *IEEE Transactions on Haptics*, vol. 8, no. 4, pp. 454–466, Oct. 2015, conference Name: IEEE Transactions on Haptics.

[20] F. Aggogeri, T. Mikolajczyk, and J. O'Kane, "Robotics for rehabilitation of hand movement in stroke survivors," *Advances in Mechanical Engineering*, vol. 11, no. 4, p. 1687814019841921, Apr. 2019, publisher: SAGE Publications. [Online]. Available: https://doi.org/10.1177/1687814019841921

[21] C. Pacchierotti, S. Sinclair, M. Solazzi, A. Frisoli, V. Hayward, and D. Prattichizzo, "Wearable Haptic Systems for the Fingertip and the Hand: Taxonomy, Review, and Perspectives," *IEEE Transactions on*

Haptics, vol. 10, no. 4, pp. 580–600, Oct. 2017, conference Name: IEEE Transactions on Haptics.

[22] W. R. Provancher and N. D. Sylvester, "Fingerpad Skin Stretch Increases the Perception of Virtual Friction," *IEEE Transactions on Haptics*, vol. 2, no. 4, pp. 212–223, Oct. 2009, conference Name: IEEE Transactions on Haptics.

[23] S. B. Schorr and A. M. Okamura, "Fingertip Tactile Devices for Virtual Object Manipulation and Exploration," in *Proceedings of the 2017 CHI Conference on Human Factors in Computing Systems*, ser. CHI '17. New York, NY, USA: Association for Computing Machinery, May 2017, pp. 3115–3119. [Online]. Available: https://doi.org/10.1145/3025453.3025744

[24] R. S. Johansson and G. Westling, "Roles of glabrous skin receptors and sensorimotor memory in automatic control of precision grip when lifting rougher or more slippery objects," *Experimental Brain Research*, vol. 56, no. 3, pp. 550–564, Oct. 1984. [Online]. Available: https://doi.org/10.1007/BF00237997

[25] P. Jenmalm, C. Schmitz, H. Forssberg, and H. H. Ehrsson, "Lighter or Heavier Than Predicted: Neural Correlates of Corrective Mechanisms during Erroneously Programmed Lifts," *Journal of Neuroscience*, vol. 26, no. 35, pp. 9015–9021, Aug. 2006, publisher: Society for Neuroscience Section: Articles. [Online]. Available: https://www.jneurosci.org/content/26/35/9015

[26] P. P. Urban, T. Wolf, M. Uebele, J. J. Marx, T. Vogt, P. Stoeter, T. Bauermann, C. Weibrich, G. D. Vucurevic, A. Schneider, and J. Wissel, "Occurence and Clinical Predictors of Spasticity After Ischemic Stroke," *Stroke*, vol. 41, no. 9, pp. 2016–2020, Sep. 2010, publisher: American Heart Association. [Online]. Available: https://www.ahajournals.org/doi/full/10.1161/STROKEAHA.110.581991

[27] D. E. Levac, M. E. Huber, and D. Sternad, "Learning and transfer of complex motor skills in virtual reality: a perspective review," *Journal of NeuroEngineering and Rehabilitation*, vol. 16, no. 1, p. 121, Oct. 2019. [Online]. Available: https://doi.org/10.1186/s12984-019-0587-8

[28] D. Leonardis, M. Solazzi, I. Bortone, and A. Frisoli, "A 3-RSR Haptic Wearable Device for Rendering Fingertip Contact Forces," *IEEE Transactions on Haptics*, vol. 10, no. 3, pp. 305–316, Jul. 2017, conference Name: IEEE Transactions on Haptics.

[29] K. Minamizawa, S. Fukamachi, H. Kajimoto, N. Kawakami, and S. Tachi, "Gravity grabber: wearable haptic display to present virtual mass sensation," in *ACM SIGGRAPH 2007 emerging technologies*, ser. SIGGRAPH '07. New York, NY, USA: Association for Computing Machinery, Aug. 2007, pp. 8–es. [Online]. Available: https://doi.org/10.1145/1278280.1278289

[30] Z. F. Quek, S. B. Schorr, I. Nisky, A. M. Okamura, and W. R. Provancher, "Augmentation Of Stiffness Perception With a 1-Degree-of-Freedom Skin Stretch Device," *IEEE Transactions on Human-Machine Systems*, vol. 44, no. 6, pp. 731–742, Dec. 2014, conference Name: IEEE Transactions on Human-Machine Systems.

[31] N. Nakazawa, R. Ikeura, and H. Inooka, "Characteristics of human fingertips in the shearing direction," *Biological Cybernetics*, vol. 82, no. 3, pp. 207–214, Feb. 2000. [Online]. Available: https://doi.org/10.1007/s004220050020

[32] M. Wiertlewski and V. Hayward, "Mechanical behavior of the fingertip in the range of frequencies and displacements relevant to touch," *Journal of Biomechanics*, vol. 45, no. 11, pp. 1869–1874, Jul. 2012. [Online]. Available: https://www.sciencedirect.com/science/article/pii/S0021929012003260

[33] F. E. van Beek, R. J. King, C. Brown, M. D. Luca, and S. Keller, "Static Weight Perception Through Skin Stretch and Kinesthetic Information: Detection Thresholds, JNDs, and PSEs," *IEEE Transactions on Haptics*, vol. 14, no. 1, pp. 20–31, Jan. 2021, conference Name: IEEE Transactions on Haptics.

[34] Y. Kamikawa and A. M. Okamura, "Comparison Between Force-Controlled Skin Deformation Feedback and Hand-Grounded Kinesthetic Force Feedback for Sensory Substitution," *IEEE Robotics and Automation Letters*, vol. 3, no. 3, pp. 2174–2181, Jul. 2018, conference Name: IEEE Robotics and Automation Letters.

[35] R. Rätz, R. M. Müri, and L. Marchal-Crespo, "Design of a Haptic Palmar Device with Thumb Flexion and Circumduction Movements for Sensorimotor Stroke Rehabilitation," in *2022 44th Annual International Conference of the IEEE Engineering in Medicine & Biology Society (EMBC)*, Jul. 2022, pp. 2644–2647, iSSN: 2694-0604.

[36] K. Minamizawa, D. Prattichizzo, and S. Tachi, "Simplified design of haptic display by extending one-point kinesthetic feedback to multipoint tactile feedback," in *2010 IEEE Haptics Symposium*, Mar. 2010, pp. 257–260, iSSN: 2324-7355.

[37] G. Buckingham, J. S. Cant, and M. A. Goodale, "Living in A Material World: How Visual Cues to Material Properties Affect the Way That We Lift Objects and Perceive Their Weight," *Journal of Neurophysiology*, vol. 102, no. 6, pp. 3111–3118, Dec. 2009, publisher: American Physiological Society. [Online]. Available: https://cir.nii.ac.jp/crid/1363107369805314304

[38] G. A. Gescheider, *Psychophysics: The Fundamentals*, 3rd ed. New York: Psychology Press, May 1997.

[39] L. A. Jones, "Perception of force and weight: Theory and research," *Psychological Bulletin*, vol. 100, pp. 29–42, 1986, place: US Publisher: American Psychological Association.

[40] W. N. Lim, K. M. Yap, Y. Lee, C. Wee, and C. C. Yen, "A Systematic Review of Weight Perception in Virtual Reality: Techniques, Challenges, and Road Ahead," *IEEE Access*, vol. 9, pp. 163 253–163 283, 2021, conference Name: IEEE Access.

[41] E. E. Brodie and H. E. Ross, "Sensorimotor mechanisms in weight discrimination," *Perception & Psychophysics*, vol. 36, no. 5, pp. 477–481, Sep. 1984. [Online]. Available: https://doi.org/10.3758/BF03207502

[42] K. Matsui, S. Okamoto, and Y. Yamada, "Relative Contribution Ratios of Skin and Proprioceptive Sensations in Perception of Force Applied to Fingertip," *IEEE Transactions on Haptics*, vol. 7, no. 1, pp. 78–85, Jan. 2014, conference Name: IEEE Transactions on Haptics.

[43] C. Giachritsis, J. Barrio, M. Ferre, A. Wing, and J. Ortego, "Evaluation of weight perception during unimanual and bimanual manipulation of virtual objects," in *World Haptics 2009 - Third Joint EuroHaptics conference and Symposium on Haptic Interfaces for Virtual Environment and Teleoperator Systems*, Mar. 2009, pp. 629–634.

[44] E. H. Weber, "The sense of touch and common feeling, 1846," in *Readings in the history of psychology*, ser. Century psychology series. East Norwalk, CT, US: Appleton-Century-Crofts, 1948, pp. 194–196.

[45] C. Giachritsis, R. Wright, and A. Wing, "The Contribution of Proprioceptive and Cutaneous Cues in Weight Perception: Early Evidence for Maximum-Likelihood Integration," in *Haptics: Generating and Perceiving Tangible Sensations*, ser. Lecture Notes in Computer Science, A. M. L. Kappers, J. B. F. van Erp, W. M. Bergmann Tiest, and F. C. T. van der Helm, Eds. Berlin, Heidelberg: Springer, 2010, pp. 11–16.

[46] P. Preechayasomboon, A. Israr, and M. Samad, "Chasm: A Screw Based Expressive Compact Haptic Actuator," in *Proceedings of the 2020 CHI Conference on Human Factors in Computing Systems*. Honolulu HI USA: ACM, Apr. 2020, pp. 1–13. [Online]. Available: https://dl.acm.org/doi/10.1145/3313831.3376512

[47] H. Wang, G. De Boer, J. Kow, A. Alazmani, M. Ghajari, R. Hewson, and P. Culmer, "Design Methodology for Magnetic Field-Based Soft Tri-Axis Tactile Sensors," *Sensors*, vol. 16, no. 9, p. 1356, Sep. 2016, number: 9 Publisher: Multidisciplinary Digital Publishing Institute. [Online]. Available: https://www.mdpi.com/1424-8220/16/9/1356

[48] T. P. Tomo, S. Somlor, A. Schmitz, L. Jamone, W. Huang, H. Kristanto, and S. Sugano, "Design and Characterization of a Three-Axis Hall Effect-Based Soft Skin Sensor," *Sensors*, vol. 16, no. 4, p. 491, Apr. 2016, number: 4 Publisher: Multidisciplinary Digital Publishing Institute. [Online]. Available: https://www.mdpi.com/1424-8220/16/4/491

[49] T. Le Signor, N. Dupré, and G. F. Close, "A Gradiometric Magnetic Force Sensor Immune to Stray Magnetic Fields for Robotic Hands and Grippers," *IEEE Robotics and Automation Letters*, vol. 7, no. 2, pp. 3070–3076, Apr. 2022, conference Name: IEEE Robotics and Automation Letters.

[50] J. O. Templeman, B. B. Sheil, and T. Sun, "Multi-axis force sensors: A state-of-the-art review," *Sensors and Actuators A: Physical*, vol. 304, p. 111772, Apr. 2020. [Online]. Available: https://www.sciencedirect.com/science/article/pii/S0924424719308842

[51] H.-K. Lee, J. Chung, S.-I. Chang, and E. Yoon, "Real-time measurement of the three-axis contact force distribution using a flexible capacitive polymer tactile sensor," *Journal of Micromechanics and Microengineering*, vol. 21, no. 3, p. 035010, Feb. 2011. [Online]. Available: https://dx.doi.org/10.1088/0960-1317/21/3/035010

[52] K. Larson, "Can You Estimate Modulus From Durometer Hardness for Silicones?" DOW, Midland, Michigan, United States, White paper, 2019. [Online]. Available: https://www.dow.com/content/dam/dcc/documents/en-us/tech-art/11/11-37/11-3716-01-durometer-hardness-for-silicones.pdf

[53] N. G. McCrum, C. P. Buckley, and C. B. Bucknall, *Principles of polymer engineering*, ser. Oxford science publications. Oxford: Oxford University Press, 1996.

[54] U. of Cambridge, "Viscoelasticity and hysteresis," Apr. 2006. [Online]. Available: https://www.doitpoms.ac.uk/tlplib/bioelasticity/viscoelasticity-hysteresis.php

[55] A. Dwivedi, A. Ramakrishnan, A. Reddy, K. Patel, S. Ozel, and C. D. Onal, "Design, Modeling, and Validation of a Soft Magnetic 3-D Force Sensor," *IEEE Sensors Journal*, vol. 18, no. 9, pp. 3852–3863, May 2018, conference Name: IEEE Sensors Journal. [Online]. Available: https://ieeexplore.ieee.org/abstract/document/8314107

[56] Q. Nie and F. C. Sup, "A Soft Four Degree-of-Freedom Load Cell Based on the Hall Effect," *IEEE Sensors Journal*, vol. 17, no. 22, pp. 7355–7363, Nov. 2017, conference Name: IEEE Sensors Journal. [Online]. Available: https://ieeexplore.ieee.org/abstract/document/8047967

[57] T. Le Signor, N. Dupré, J. Didden, E. Lomakin, and G. Close, "Mass-Manufacturable 3D Magnetic Force Sensor for Robotic Grasping and Slip Detection," *Sensors*, vol. 23, no. 6, p. 3031, Jan. 2023, number: 6 Publisher: Multidisciplinary Digital Publishing Institute. [Online]. Available: https://www.mdpi.com/1424-8220/23/6/3031

[58] D. A. Winter, *Biomechanics and Motor Control of Human Movement*. John Wiley & Sons, Oct. 2009, google-Books-ID: _bFHL08IWfwC.

A

Design Notes

This section introduces additional information on the design process for the tactile interface. The standard mechatronic system design workflow has been followed, starting with the definition of the system requirements, moving on with the functional design of the system, following with the specific component requirements, and concluding with the integration and evaluation of the whole system. While some aspects have already been presented in chapter 2, they may be touched upon again to provide a complete overview of the workflow.

A.1. System requirements

The starting point of the design comprised the definition of the requirements that the system should comply with. As discussed in the paper presented in chapter 2, multiple requirements stemmed from the fact that the tactile interface developed in this thesis was meant to be incorporated in a larger haptic device for hand rehabilitation [5]. Additionally, numerous requirements were used to define the desired response and capabilities of the system, based on insights provided by literature on haptics and human perception (see chapter 2). In addition to the requirements summarized in Table A.1, maintaining a low cost of manufacturing was considered a major requirement in the design

Table A.1: Summary of system requirements

Requirements for integration into the hand rehabilitation robot (Integration Requirements)	
IR-01	The design should continue to allow a range of motion of the fingers from $0°$ to $165°$.
IR-02	The design should continue to allow the setup of the user's hand into the hand rehabilitation robot in a closed position.
IR-03	The design should have minimal impact on the range of motion of the thumb.
IR-04	Tactile stimuli should match the actuation provided by the robot, that is simultaneous actuation of all fingers but the thumb.
Requirements on desired capabilities of the interface (Design Requirements)	
DR-01	The actuation of the system should cover the entire plane tangential to the finger pads.
DR-02	The system should be able to render forces as large as 5 N.
DR-03	The accuracy for rendering forces should be lower than 0.05 N for forces below 1.5 N, and lower than 0.1 N otherwise.
DR-04	The desired forces should be rendered by the device in less than 0.35 s.
DR-05	The device should be able to stretch the skin up to 5 mm.

A.2. Functional description

Considering the size constraints imposed by IR-01, IR-02, and IR-03, a design similar to the previous end effector of the haptic device was selected. To comply with IR-04, the interface was envisioned as a moving platform upon which the finger pads would rest. The movement of the platform would deform the finger pads, reproducing the naturally occurring skin stretch caused by tangential forces [6]. Contrary to wearable devices, the fingers are not grounded at the interface but at the finger fixation component of the hand rehabilitation robot.

Figure A.1: Mock-ups used for comparing the sensation provided by a fully actuated platform and a multidigit tactor-like design with a frame for grounding the outer area of the finger pads.

A preliminary qualitative test was conducted to evaluate whether the grounding approach was sufficient. Manually actuated mock-ups were designed for this purpose, one with a platform upon which the entire fingerpads would rest, and another with a frame to provide grounding to the outer part of the finger pads (see Figure A.1), similar to tactor-based skin stretch interfaces [1]. During the test, the tactor-like design was perceived to be more uncomfortable, occasionally pinching the skin, and providing an overall "*unnatural*" sensation. Thus, the platform design was selected for future versions.

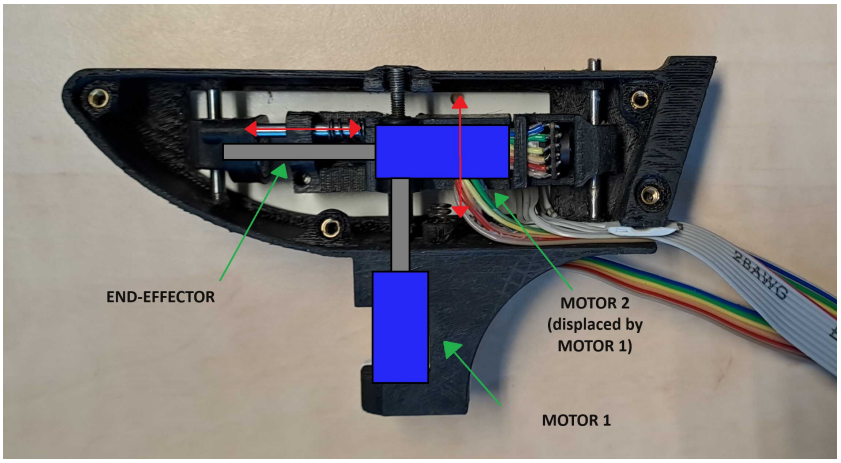

Figure A.2: Simplified view of the mechanism. MOTOR 2 is directly connected to the end-effector and provides motion in the mediolateral direction of the hand. MOTOR 1 displaces the whole second axis of the mechanism and with it, the end-effector, in the proximo-distal direction.

To satisfy DR-01, the system needed to be actuated in two degrees of freedom. This was achieved through a pair of linear actuators orthogonally mounted in a serial configuration, with the platform attached to the moving component of the vertical motor (MOTOR 2 in Figure A.2). Compared to parallel planar mechanisms, this disposition resulted in simpler kinematics, more uniform displacements and forces over the plane of actuation, and an overall smaller size of the interface.

To achieve an accurate realization of the forces, it was opted for using a force sensor connected between the moving component of the vertical axis and the platform stretching the finger pads. Such a location allows the measurement of the applied force without influence from the friction and the damping in the mechanism.

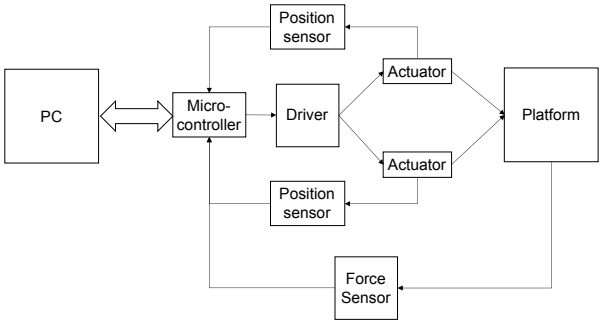

Figure A.3: Functional diagram depicting the building blocks of the system and the necessary connections (or information-passing channels) among them.

Once the high-level design of the system is defined, a functional diagram of the system with the necessary building blocks is created. Such a diagram allows the identification of the components of the system, as well as the connections between them. Figure A.3 depicts the functional diagram of the tactile interface, with a microcontroller interfacing with the computer to control the actuators through associated drivers. In addition to force sensor measurements, information from the position of the actuators is also fed back to the microcontroller. Doing so allows to control potential slip between the platform and the fingers and to avoid reaching the actuation limits of the mechanism.

A.3. Component requirements

The following step in the design of the system is to define the specifications needed to select the physical components that will be used in the actual device. To do so, the system requirements previously defined are refined into component-level requirements. The most critical components to achieve the specified requirements are the actuators and the force sensor. The details, requirements, and design of the force sensor are provided in chapter 2. Therefore, this section will focus on the definition of the requirements for the actuators. Some of the other requirements, like the encoders and drivers, will be selected later on based on the specifications of the selected motor.

A.3.1. Actuator

At this point, different alternatives for the actuation had been considered and compared. A leadscrew actuation was selected for the reasons described in chapter 2. In order to compute the requirements for the actuator, the specifications of the leadscrew for the transmission from rotational to linear motion are needed. A conventional M3 threaded rod with 0.5 mm/rev lead was selected for this purpose.

To determine the speed of the motor, we consider the temporal requirement of the interface (DR-03), and the range of motion requirement (DR-05). Based on these, the system should be able to displace up to 5 mm in a lapse of 0.35 s. We assume a step response of the actuator, considering that the time needed to reach steady-state velocity is negligible. Therefore, a constant velocity can be assumed throughout the displacement.

Those values yield a linear velocity of 14.28 mm/s. Considering a lead of 0.5 mm/rev for the threaded rod used for the leadscrew, an angular velocity of 28.57 rps, or 1714.3 rpm is obtained. By factoring a safety margin of 1.5, a 2400 rpm velocity is obtained.

In order to compute the maximum torque required by the motor, we consider the distribution of the forces in the leadscrew. This can be done by simplifying the leadscrew as a slope, as depicted in Figure A.4. The simplified slope has an elevation equal to the lead (l) and a length equal to the length of the cross-section of the leadscrew (a circle with a diameter equal to the pitch diameter of the screw, $\pi\, D_p$). The resulting inclination of the slope can be computed as $\lambda = \arctan\, l/(\pi\, D_p)$.

We consider the case in which a force F_{des} of 5 N, acting in the longitudinal direction of the leadscrew, needs to be exerted by the actuator. Due to the inclination of the platform, the exerted force F_{des} causes a normal force (N) perpendicular to the slope and a subsequent friction force ($\mu\, N$) on the surface. The corresponding force applied by the motor on the thread (slope), denoted as F_{app}, should be enough to overcome said friction in the system.

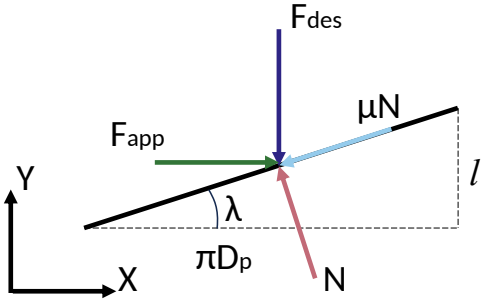

Figure A.4: Diagram of the forces acting on the leadscrew.

By decomposing the forces along the X and Y axes (see Figure A.4), it is possible to obtain an expression (A.1) for the force that needs to be applied (F_{app}) to overcome the desired force (F_{des}). Considering the relation between the torque of the motor (τ) and the applied force, $F_{app} = 2\tau/D_p$, one obtains the expression for the required torque (A.2).

$$F_{app} = \frac{F_{des}\,(l + \mu\pi\, D_p)}{\pi\, D_p - \mu l} \tag{A.1}$$

$$\tau = \frac{F_{des} D_p}{2}\left(\frac{l + \mu\pi\, D_p}{\pi\, D_p - \mu l}\right) \tag{A.2}$$

One final correction needs to be performed to this last expression. Metric threads do not have a flat or square thread, but a V-shaped one. As a result, the surface of the thread is increased, and with it, the friction force. The correction can be applied by factoring in the thread angle (α), equal to half of the angle between the flanks of the thread. The corrected expression for the required torque is then obtained (A.3).

$$\tau = \frac{F_{des} D_p}{2}\left(\frac{l + \mu\pi\, D_p \sec\alpha}{\pi\, D_p - \mu l \sec\alpha}\right) \tag{A.3}$$

To finally compute the value, we consider $F_{des} = 5$ N, $D_p = 2.65$ mm, $l = 0.5$ mm/rev, and $\alpha = 30°$. As for the friction coefficient, we consider a range between 0.2 and 0.5, which are ranges commonly found depending on the lubrication conditions, among others. The resulting torque values span the range of 1.955–4.375 N mm, of 0.2–0.446 kgf mm. The upper bound of this value will be considered for the selection of the actuator.

A.4. Component selection and Bill of Materials

With the component-level specifications defined, a search for matching items was performed through multiple electronic and mechanical component suppliers. The resulting bill of materials is shown in Table A.2. For some of the components, like the motor drivers and the voltage regulator, off-the-shelf breakout boards are listed. The reason for such a choice was their ease of assembly and testing during

the initial prototyping stages. The selection of some components, like the DC motors, was driven by market availability and budget constraints. Other components that are required for connectivity and assembly have also been included to provide a complete bill of materials for the device.

A.5. System integration & evaluation

Once the components have been selected, it is necessary to connect them both physically and electronically to realize the whole system and evaluate whether the requirements have been met. Since the integration of the components comprises multiple layers of design and fabrication, separate appendices have been dedicated to each of them.

The electronic connection between the microcontroller, the drivers, and the sensors and actuators was carried out through custom-made printed circuit boards (PCBs). The design of the boards is presented in Appendix B. The assembly of the mechanism and the actuators themselves comprised the use of multiple custom 3D-printed and mechanical parts. Furthermore, the force sensor was completely manufactured in-house. The details of these manufacturing and assembly processes can be found in Appendix C. Finally, the software necessary for the microcontroller was implemented in embedded C++. The details on the architecture and its implementation into the microcontroller can be found in Appendix D. The evaluation of the resulting device was presented in chapter 2, although more details are available in Appendix E.

Table A.2: Bill of materials of the tactile haptic interface

Item	Description	Manufacturer	Part number	Quantity
Actuator	6V 5:1 micro metal gearmotor HPCB	Pololu (US)	3082	2
Threaded rod	M3x30 mm threaded rod to be used as leadscrew	Off-the-shelf	-	2
Brass inserts	M3x5.4 mm brass inserts for assembly and leadscrew nut	TR fastenings (UK)	M3-UHBRHESF	11
Linear bearing	3 x 7 x 10 mm linear ball bearing for X-axis support axles	Misumi (Germany)	C-LMU3	2
Annular bearing	Ring ball bearing for Y-axis leadscrew support	Conrad (The Netherlands)	623-ZZ	1
Slide bearing	3 x 5 x 7 mm slide bearing, for Y-axis support axle	Ferrofast (The Netherlands)	A36802	1
Support axles	3 mm stainless steel rods, for support axles	Misumi (Germany)	SSFHR3-150	2 (cut as needed)
Encoder	12 count-per-revolution magnetic encoders, for motor position sensing	Pololu (United States)	3081	1 (pair)
Driver	DRV8876 (Texas Instruments, United States) brushed DC motor driver	Pololu (United States)	4036	2
MCU	ESP32 Devkit-V1 microcontroller development board	Espressif (China)	ESP32 Devkit-V1	1
Magnetometer	MLX90393 three-axis magnetometer, for use in force sensor	Melexis (Belgium)	MLX90393 SLW	1
Silicone	Dragon Skin 30 two-component silicone, for use in force sensor	Smooth-On (United States)	-	1
Magnet	3 x 1 mm N48 cylindrical magnet, for use in force sensor	MagnetPartner (Denmark)	MAGZ-087-P	1
Capacitors	0.1 μF capacitors for decoupling magnetometer chip	Samsung (South Korea)	CL05A104-KA5NNNC	2
6-pin header	Cable connector header, for motor connection	JST (Japan)	XHP-6	2
6-pin housing	Cable connector housing, for motor connection	JST (Japan)	S6B-XH-A	2
8-pin header	Cable connector header, for sensor connection	JST (Japan)	XHP-8	1
8-pin housing	Cable connector housing, for sensor connection	JST (Japan)	S8B-XH-A	1
Barrel header	Barrel jack connector plug, for power supply	CUI Devices (United States)	PP3-002A	1
Barrel housing	Barrel jack connector housing, for power supply	CUI Devices (United States)	PJ-102AH	1
Voltage regulator	6V voltage regulator D36V28F6, to provide power to the actuators	Pololu (United States)	3783	1
Screws	M1.6 and M3 screws for connection of components			Multiple M1.6–M3
Flat cable	6- and 8-wire cable, for sensor and actuator connection to PCB	Off-the-shelf	-	1 m
3D printing filament	GreenTEC anthracite/white filament, FDA-approved. For manufacturing of custom parts	Extrudr (Austria)	-	1.1 kg

B

Printed Circuit Board Design

Two Printed Circuit Boards (PCBs) were designed for the system. In this section, details on the steps and the intermediate outputs of the PCB design process are presented. The schematic designs with the connection of the components of the system are first introduced, followed by the considerations taken for the physical layout of the boards, including the necessary calculations for the traces.

One of the PCBs, to which we refer as the *main electronics PCB*, was designed to connect the microcontroller to the power, control, sensing, and actuating elements of the system. Doing so allows for robust electrical connections, reduced electrical noise in communication lines, and easier assembly into the hand rehabilitation robot. Its design aimed to reuse existing components used for prototyping and ensure simple manufacturing. As a result, breakout boards for the voltage regulator and motor drivers were used despite the increased volume of the assembled board.

The second PCB, to which we refer as the *sensor PCB*, was created to accommodate the 3-axis magnetometer chip into the interface. Due to the reduced space available within the tactile interface, the use of off-the-shelf boards for the selected chip was not possible. Aiming for reduced manufacturing costs, the board was designed to fit in either a left- or right-hand module with minor changes in the design of the 3D-printed parts to which it is easily connected with a pair of screws.

B.1. Schematics

The initial stage of PCB design comprised the schematic design of the connections between the components of the board and the connectors needed to interface with sensors and actuators. Full-page-sized versions of the schematics can be found in Appendix G.

B.1.1. Main electronics PCB schematic

Figure B.1a illustrates the schematic design of the board for the power and control electronics. The ESP32, depicted at the right of the schematic, is wired to the DRV8876 driver boards and the connectors for the custom force sensor and the actuators. Input sockets for the provision of power can be found at the top-left of the diagram, together with headers for the 6V regulator used to increase the range of input voltages that can be provided to the system. Additional connectivity with unused pins of the ESP32 and DRV8876 boards was also included for future extension of peripherals or system functionalities.

B.1.2. Force sensor PCB schematic

The schematic design of the PCB for the magnetic sensor is shown in Figure B.1b. The magnetometer chip, depicted in the center of the figure, is wired following the indications of the manufacturer for a 4-wire SPI communication protocol. Unconnected pins and I2C selection pins are connected to the ground of the circuit, and decoupling capacitors of 0.1 µF are placed next to the positive voltage power terminals. The connectors to the right provide connectivity for powering and interfacing with the sensor.

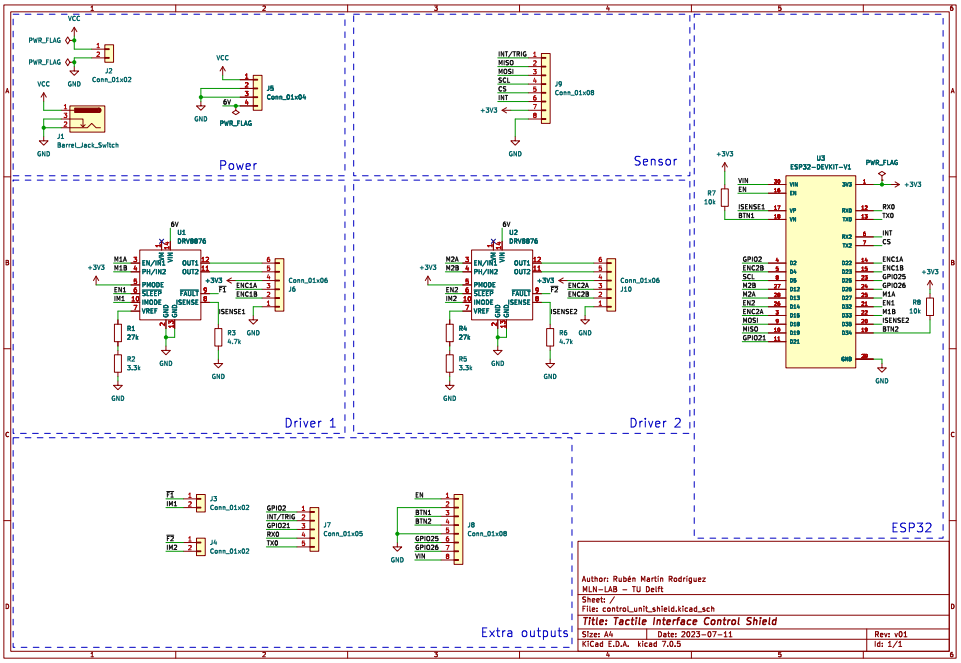

(a)

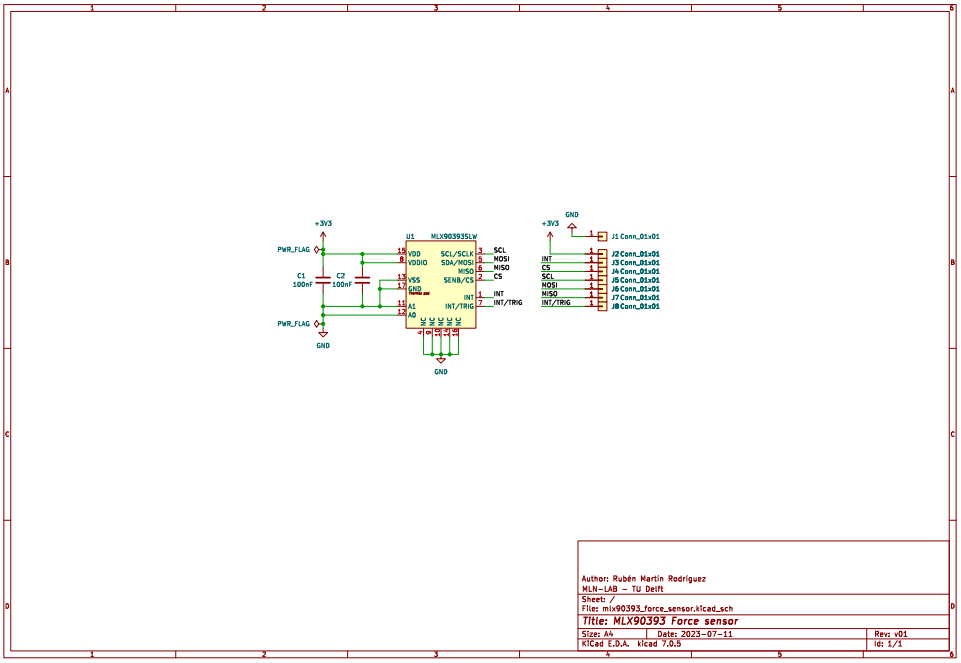

(b)

Figure B.1: (a) Schematic design of the PCB containing the control, power, and communication electronics for the system. (b) Schematic design of the PCB for the 3-axis magnetic sensor chip.

B.2. Layouts

With the connections between components defined, the physical design of the boards was performed. This comprised the dimensioning of the boards, mounting points, distribution of the components and connectors across the board, and most importantly, the routing of the copper traces between component terminals. The footprints used in the layout correspond to the components listed in section A.4.

B.2.1. Main electronics PCB layout

The design of the main electronics PCB was carried out considering the desired location of the PCB within the hand rehabilitation robot. The finger fixation part in the robot, pressing against the back of the fingers, was selected for its close distance to the mechanism without affecting the range of motion of the finger flexion or the thumb. Reducing the length of the cables running to the sensors and actuators helped reduce the potential impact of interferences or noise in the readings of the encoders and the high-speed communication with the magnetic sensor.

To install the PCB, M3 mounting holes were placed in the corners of the PCB, as shown in Figure B.2a. The connectors for peripheral components, power, and communication, were distributed across the board to facilitate the wiring when mounting the system into the hand rehabilitation robot. Finally, the through-hole mounting of the components allowed to place components on both sides of the PCB. By doing so, the overall size of the board was reduced to 54.35 x 82.80 mm.

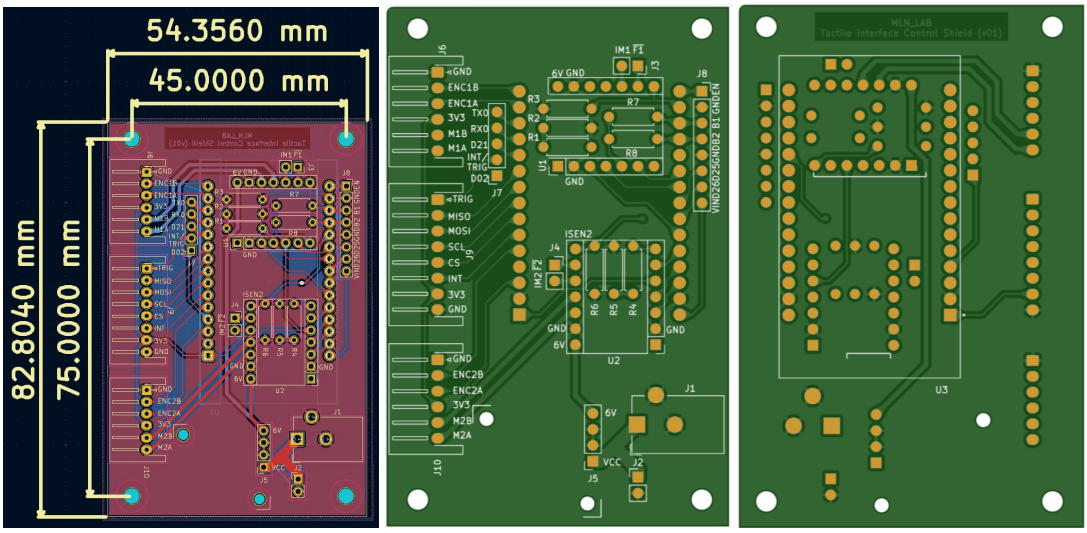

Figure B.2: Layout of the power and control electronics PCB. (a) CAD view and dimensions of the control and electronics PCB. (b), (c) Top and bottom views of the final layout of the board

Special attention was paid to the copper traces providing power to the drivers and the motors. The maximum 1.5 A stalling current from the selected motors translates into a theoretical maximum current of 3 A flowing through between the power input and the converter, and 1.5 A between the driver and motor. When large currents flow through PCB traces, they can heat up and expand, potentially damaging the board. By increasing the width of the trace and with it, the cross-section of the conductor, the temperature rise is reduced. The calculation of the trace area A and width W is based on estimated formulas from the IPC-2221 standard.

$$A = \left(\frac{I}{k \times {T_{Rise}}^{b}} \right)^{1/c} \tag{B.1}$$

$$W = \frac{A}{t \times 1.378} \tag{B.2}$$

A typical value of $T_{Rise} = 10°C$ and a trace thickness $t = 1\,oz$ was considered. Since the traces are external (i.e. only on the top and bottom copper layers), the constant values $k = 0.048$, $b = 0.44$, and $c = 0.725$ were taken, as indicated in IPC-2221. With these values, and for maximum currents of 1.5 A and 3 A, trace widths of 0.525 mm and 1.367 mm were obtained. A safety margin of 1.5 was considered to account for variations in environmental conditions from the estimated ones, resulting in trace widths of 0.75 mm and 2 mm for the motor power traces and power supply traces, respectively.

B.2.2. Force sensor PCB layout

The design of the PCB for the 3-axis magnetometer aimed for a compact design that would fit within the available space in the mechanism. The resulting board, of 16.0 x 17.4 mm (see Figure B.3), features three M1.6 mounting holes used for attaching the board to the mechanism and the 3D-printed connector of the elastomer part of the sensor. The holes are positioned for simple integration into the mechanism, and regardless of whether a right-hand or a left-hand version of the system is assembled.

To minimize the impact of temperature variations on the magnetometer readings, heat dissipation was promoted by connecting its thermal pad to the ground of the circuit. Temperature invariance was further promoted through the use of thermal vias beneath the thermal pad of the chip. These vias connect the ground planes of the top and bottom copper layers, increasing the amount of material connected to the thermal pad and so, reducing the heat fluctuations in the sensing unit. Finally, surface-mounted terminals were selected for the communication and power cable due to their compact size and sufficient robustness with the help of external stress reliefs in the cable.

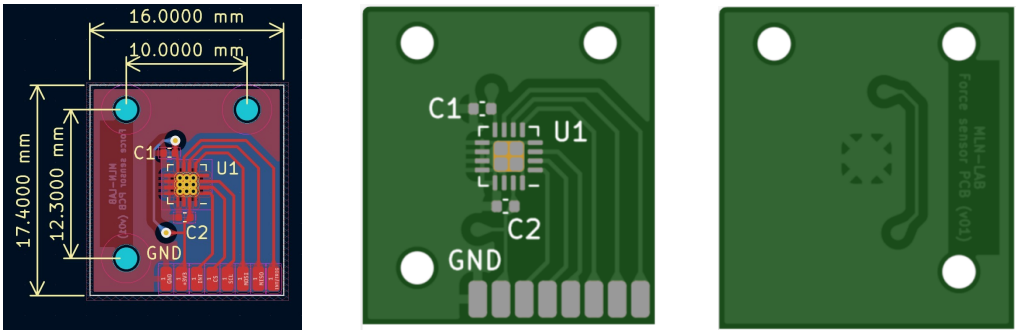

Figure B.3: Layout of the magnetic sensor PCB. (a) CAD view and dimensions of the sensor PCB. (b), (c) Top and bottom view of the final layout for the sensor board.

B.3. Results

The PCBs were manufactured using 1 oz/sq.ft. layer thickness on both sides of an FR-4 rigid substrate of 1.6 mm thickness. The resulting boards are depicted in Figure B.4.

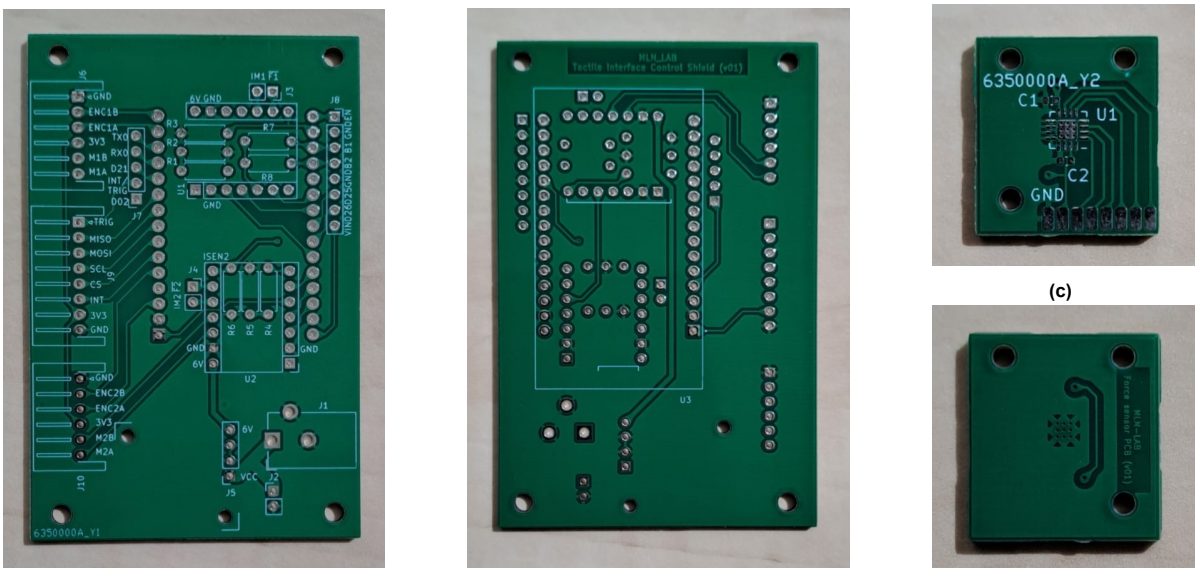

Figure B.4: Manufactured PCBs, before assembly. (a), (b) Top and bottom views of the manufactured power and control PCB. (c), (d) Top and bottom views of the manufactured magnetic sensor PCB.

C

Manufacturing

The present section contains additional information on the manufacturing of the tactile interface and the force sensor. While the system used multiple off-the-shelf components, many others were made or modified in-house. The specifications of the materials and dimensions of customized components and assemblies are presented, together with the steps taken to produce them.

Figure C.1: Picture of the custom 3D printed parts required to assemble the tactile interface.

C.1. Housing and connecting parts

The device contains nine custom 3D-printed parts for housing and supporting the overall mechanism, as well as connecting mechanical components. These parts have been designed using Autodesk Fusion 360 and 3D-printed via fused deposition modeling (FDM) using an Ultimaker 3 (Ultimaker, Netherlands). While the initial prototypes were printed in Polylactic Acid (PLA), the final version was printed in GreenTEC Anthracite and GreenTEC White filament (Extrudr, Austria), an FDA- and RoHS-approved filament suitable for medical device manufacturing. A printing temperature of 220°C, 15% infill, and 0.15 layer height were used with both filaments. It has to be noted, though, that the thin features of many components resulted in almost solid pieces.

In addition to the nine 3D-printed components for the device depicted in Figure C.1, four parts of the original hand rehabilitation robot were modified to accommodate the tactile interface. Some regions of the tactile interface had to increase in thickness compared to the original end-effector to fit the actuators. Therefore, a cavity was introduced in the handle of the robot (Figure C.2, left) to preserve the original range of motion of the finger flexion mechanism. The length of the contact area of the thumb rest

(Figure C.2, center) was shortened to reduce the interactions with the tactile interface. Finally, mounting inserts for the PCB were introduced in the finger fixation of the robot (Figure C.2, right), which keeps the fingers in contact with the tactile interface. Due to the added volume introduced by the PCB, the locking lever of the finger fixation (Figure C.2, top-right) was lengthened to facilitate its grasping.

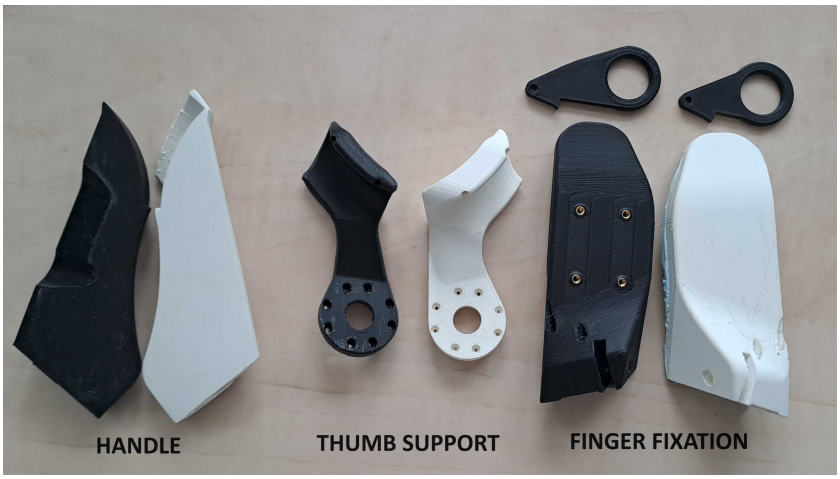

Figure C.2: Modified parts (black) next to the original counterparts (white) of the hand rehabilitation robot designed by Rätz et al. [5, 4] to improve the integration of the tactile interface into the robot.

Regarding the assembly of the 3D-printed parts, different approaches were followed attending to size constraints and the available connections in the mechanical components. M3 screws in combination with M3 x 5.8 mm brass inserts (TR Fastenings, UK) were used to connect the housing of the tactile interface to the hand rehabilitation robot, the back of the tactile interface, and the cover of the horizontal axis actuator. The linear actuators are connected via M1.6 screws to the housing and the connector between the horizontal and vertical axles. The remaining components are press-fit or screwed directly into the 3D-printed parts.

C.2. Linear actuators

The tight size constraints of the design, together with the objectives for temporal response and maximum actuation of the system, made it difficult to find off-the-shelf leadscrew-based actuators to use. While some high-end manufacturers provide motors and transmissions to build such an actuator, their elevated cost prevented their use for a prototype. Instead, conventional brushed DC motors were modified in-house to build the desired linear actuator. To do so, M3 x 30 mm stainless steel threaded rods were used as leadscrews, while the aforementioned M3 brass inserts were used as the leadscrew nuts.

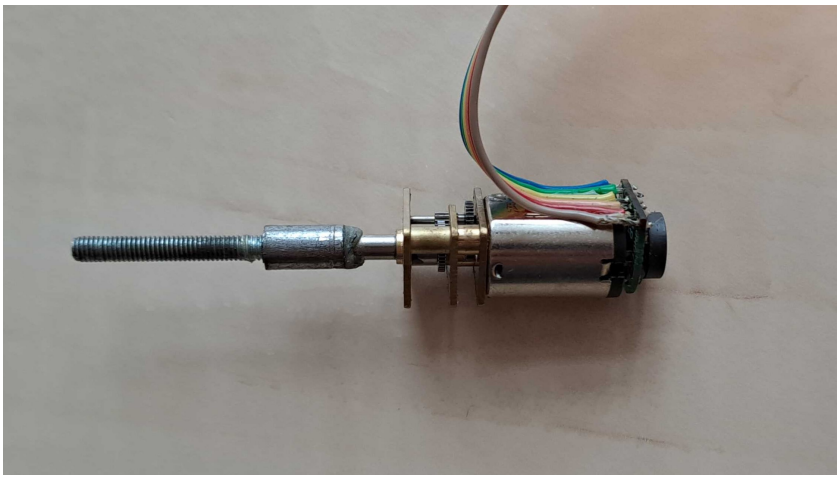

Figure C.3: Picture of the assembled actuator

To connect the threaded rod and the DC motor, a homemade coupler that would fit in the system was also manufactured. The technical drawing of the coupler with associated dimensions can be found in Appendix G. The coupler was manufactured from a 5 mm steel rod using a mechanical lathe, and features a flat hole in one end for the motor axle, and a threaded hole on the other for the threaded rod. The threaded rod was fixated using LOCTITE 243 Threadlocker glue (Henkel Loctite, United States), while the output shaft of the DC motor was attached to the other side of the coupler using 2-component epoxy resin (UHU, Germany), which was found to provide rigid connection under the torques exerted by the motor. An image of the assembled actuator is shown in Figure C.3. An exploded view and dimensions of the actuator are provided in Appendix G.

Finally, the encoders were installed in the DC motors by soldering the motor terminals to the PCB of the encoder, carefully aligning it with the rear shaft of the motor, as indicated by the manufacturer.

C.3. Electronic hardware

The Printed Circuit Boards (PCBs) presented in Appendix B were assembled in-house. For the main electronics PCB, all components and connectors featured through-hole mounting and were manually soldered. As for the sensor PCB, the small size of the surface-mounted components made it impossible to perform reliable connections by hand. Instead, a reflow soldering approach was taken, using CHIPQUIK SMD291AX50T3 soldering paste (Chipquik, Canada) and a CIF FT03 batch reflow oven (C.I.F., France) to accurately solder the components in place. The soldering paste was applied to the components using a stencil ordered from the PCB manufacturer. Once the SMD components were placed, the cables were manually soldered to the soldering pads in the PCB.

Finally, the cables for powering the device and connecting the peripherals to the main PCB were also assembled in-house. 22 AWG cable was used for the power supply, while 28 AWG flat cable with 8 and 6 wires was used for the sensor and the actuators, respectively. Each assembly used the corresponding headers and crimps specified in Appendix A. The assembled PCBs are shown in Figure C.4.

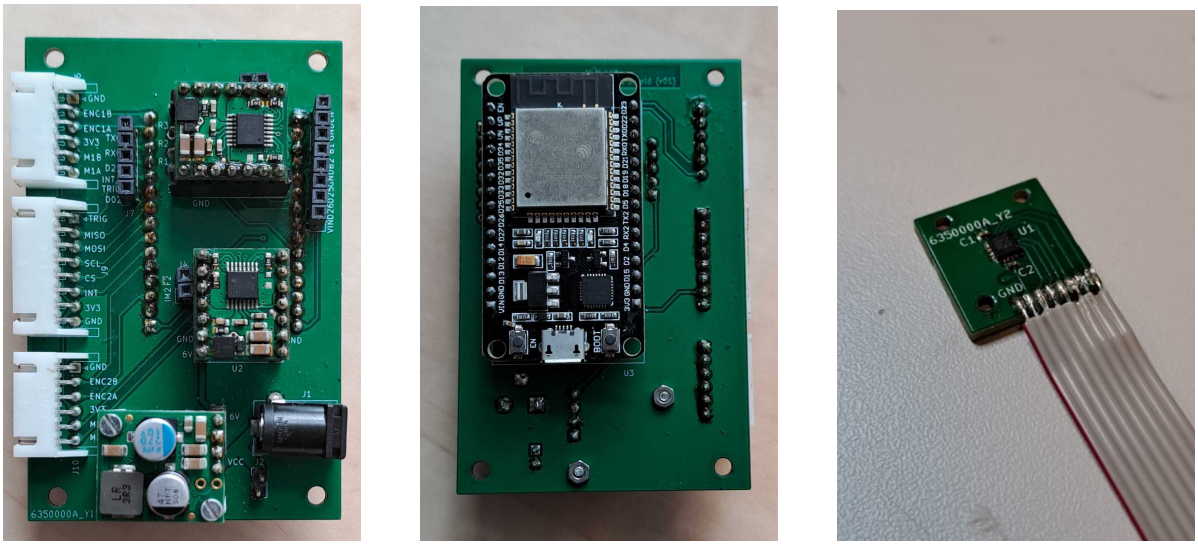

Figure C.4: Pictures of the assembled PCBs. (a), (b) Show the front and back sides of the main electronics PCB. (c) Shows the assembled PCB for the magnetic sensor with the corresponding wire.

C.4. Force sensor

As presented in previous literature on soft magnetic force sensors, the manufacturing of a force sensing unit comprises the fabrication of the PCB with the necessary electronics; the fabrication of the elastomer with the embedded magnet; and the assembly of the sensor [8, 7, 2]. Since the details on the fabrication and assembly of the PCBs can be found in Appendix B and section C.3, further information on the fabrication of the elastomer and the assembly of the sensor are provided.

The elastomer was manufactured similarly to the sensor from Wang et al. [8], using a single-step pour molding process, depicted in Figure C.5a. The mold was first prepared by applying a release agent (Ease-Release 200, Smooth-On, United States). Then, the DragonSkin 30 silicone (Smooth-On, United States) was prepared by mixing the two components, as indicated by the manufacturer, and pouring them into the mold. Once closed, the silicone was left to cure for 16 hours. After that time, the part was extracted and the magnet was placed inside. The magnet was fixed in place using Sil-poxy silicone adhesive (Smooth-On, United States), which is partially cured for 4 hours before the application of the final adhesive for assembly.

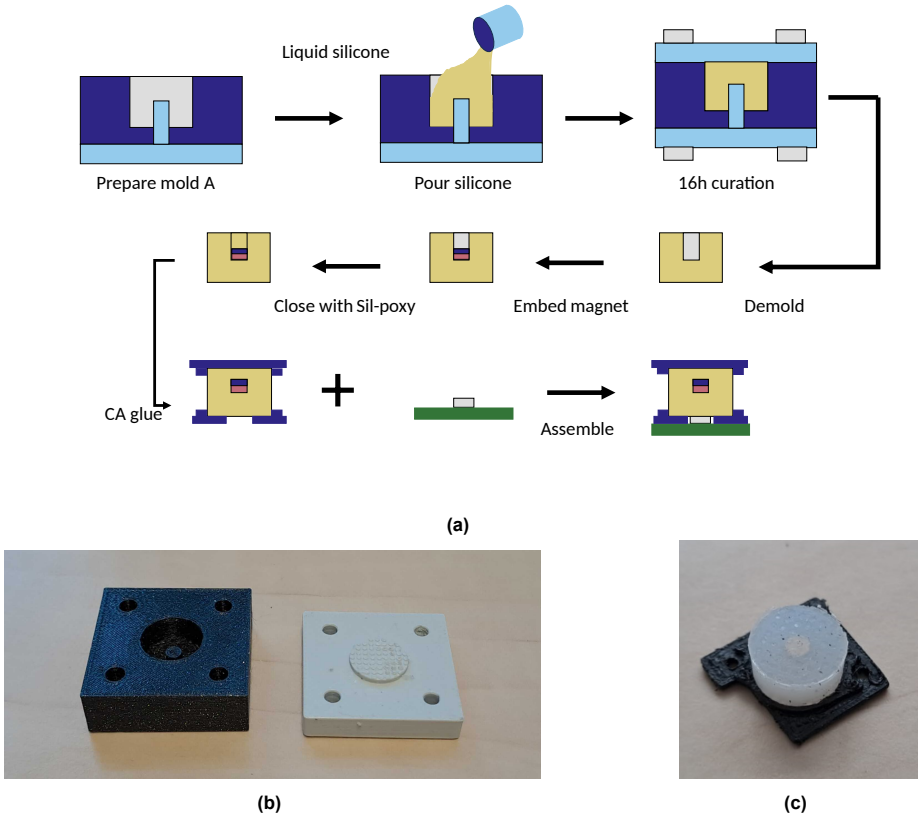

Figure C.5: (a) Process of manufacturing of the elastomer with an embedded magnet. (b) 3D-printed silicone casting molds A and B, respectively. (c) Manufactured elastomer assembled to the PCB connector.

The final step of the assembly comprised the adhesion of the elastomer, both to the 3D-printed PCB connector, and to the platform (for connection with the force/torque sensor in the case of the standalone sensor, or to deform the fingerpads, in the case of the mechanism). Some studies opted for gluing the elastomer directly to the PCB or even to the sensor itself [3] to minimize the size and variations in the relative position between the magnet and the magnetometer. However, a detachable approach was taken to facilitate assembly, maintenance, and reusability of the electronics and PCB. Different adhesives were tested, including Cyanoacrylate (CA) glue (Henkel Loctite, United States), 2-component epoxy resin (UHU, Germany), the aforementioned Si-poxy (Smooth-On, United States), and contact glue (Wakol Gmbh, Germany). The contact glue failed to adhere to the silicone, while the epoxy resin and the Sil-poxy were not capable of bearing the shear forces targeted in our application. The CA glue yielded the strongest adhesion, although a grooved pattern had to be introduced in the design of the elastomer to withstand the desired loads. Once the adhesives cured for 24 h, the silicone with the connector was attached to the PCB using the M1.6 mounting holes in the PCB and the connector.

The mold used for casting (see Figure C.5b), was 3D-printed using PLA, a layer height of 0.1 mm, and a 15% infill. A test during the initial phases of the design was carried out to compare the quality of the casted part using a pour mold and a two-part injection mold. The pour mold resulted in a more regular shape of the elastomer and minimal presence of bubbles.

D

System workflow, operation and communication

This section describes additional information about the software of the device, such as the operation and communication workflow, as well as the high-level functioning of the embedded software.

The operation of the haptic device is split into two separate loops in charge of the haptic rendering, and the communication with the computer. A graphical representation of the device operation and information transfer is provided in Figure D.1. Since the ESP32 is a dual-core microcontroller, it is possible to distribute tasks across cores, preventing critical tasks from being interrupted and lower-priority tasks from being blocked. Such a management of the tasks running in the microcontroller can be achieved in a predictable and deterministic manner by using a Real-Time Operating System (RTOS). FreeRTOS was the selected RTOS due to the support provided by Espressif for the ESP32. Such an approach also ensures the stability of the control loop to a fixed time step. One of the limitations, however, is that additional computation time is required to determine periodically which task needs to be executed and to save and restore the execution state of other tasks. Since the smallest period with which FreeRTOS performs this operation is 1 ms, it is difficult to increase the speed of the loop while keeping the frequency stable. Doing so would require the execution of multiple iterations of the loop within a single resource allocation period of the RTOS, relying instead on manual execution time management which can lead to runtime performance issues.

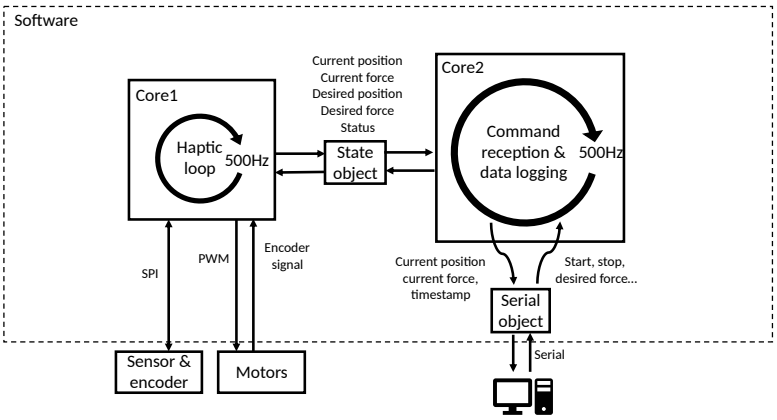

Figure D.1: Graphical representation of the tasks running in the haptic device, their distribution across hardware resources in the microcontroller, communication interfaces, and data transmitted through each of them.

In this implementation, one core is solely dedicated to the haptic loop, in charge of collecting sensor information and commanding the control action to the motors to achieve the desired positions and forces. The second core executes the reception and transmission of data over the serial port with the computer. By doing so, it is ensured that the control loop can run uninterrupted without blocking the execution of the communication loops. A single interrupt is programmed to flag the availability of data from the magnetic sensor. The execution time of the interrupt is negligible and does not impact the execution time of any of the other loops.

The communication across tasks is performed by using a class instance (represented in Figure D.1 by *State object*) that stores and passes data about the current and desired positions and forces, the timestamp and the status of the whole system. The information passed can be accessed by both cores simultaneously, which can cause some corruption in the shared data when access and store instructions take place in multiple processor cycles. While this is typically avoided using spinlocks inside higher priority tasks, or RTOS-specific objects for communication, in practice it was not found to be necessary.

Communication with physical devices depends on the hardware. The communication with the magnetic-based force sensor is performed via a 4-wire Serial Peripheral Interface (SPI) at 10 MHz. Encoder data is read through a pair of digital inputs in the ESP32, while the motors are controlled through a pair of Pulse-Width Modulated (PWM) signals. Finally, the communication for the reception of commands and transmission of data with the computer is performed via serial communication at 921.6 kbps. Data transmitted through the serial port is encoded in JavaScript Object Notation (JSON) format and parsed upon reception, which provides a simple way to modify the length and contents of the data packages.

D.1. System workflow

Upon initialization, the system executes an initial setup of the communication interfaces, the magnetic-based force sensor, the analog-to-digital converter, and control and communication tasks. Afterward, the system performs the calibration of the position sensors. Since the encoders mounted in the motors only measure relative displacements, it is necessary to determine the starting point of the range of motion of the actuator. Once finalized, the system starts operating in the way described in the previous section.

Algorithm 1 Communication loop

Require: $keys = \{"pos_x", "pos_y", "pos_{des\,x}", "pos_{des\,y}", "f_{des\,x}", "f_{des\,y}", "torque", "position", "stop"\}$
Require: $keys\_logged\_data \subseteq keys$
  $serial\_manager.receive()$
  $serial\_manager.decode()$
  for all $(key, value) \in serial\_manager.data()$ **do**
    if $key \in \{"pos_{des\,x}", "x_{des\,y}", "f_{des\,x}", "f_{des\,y}"\}$ **then**
      $robot\_state.key = value$
    else if $key \in \{"torque", "position", "stop"\}$ **then**
      $robot\_state.status = key$
    end if
  end for
  $serial\_manager.clear\_send()$
  for all $key \in keys\_logged\_data$ **do**
    $serial\_manager.send\_object().add(key, value)$
  end for
  $serial\_manager.encode()$
  $serial\_manager.send()$

The communication loop runs at a rate of 500 Hz. Whenever a command is received, the system decodes the JSON string into key-value pairs stored as a JSON Object. The task then parses each key and updates the value of the corresponding system parameter to that of the pair. Such parameters can be the robot status, the type of controller, and the desired position or force. The details of the

algorithm can be found in Algorithm 1. Afterward, the system performs the logging operation, in which key-value data pairs are sequentially added to a JSON Object. Once the JSON Object is ready, it is encoded and sent over the serial port.

One limitation of the JSON implementation is that it is very computationally intensive due to the conversion of native datatypes into strings. As a result, attempting to parse or send too much data (approximately 6 key-value pairs) resulted in the watchdog timer of the microcontroller triggering. To increase the amount of data that could be transmitted, an alternative implementation using MsgPack was inspected. While it was possible to send more data due to the more efficient packing of native datatypes, the JSON implementation was adopted for its increased stability and sufficient adequacy to our needs.

Algorithm 2 Haptic loop

Require: $magnetic\_sensor\_data\_ready = True \mid t = 0$

$new\_pos\_0 \leftarrow CountsToPosition(encoder\_0.getCount())$
$new\_pos\_1 \leftarrow CountsToPosition(encoder\_1.getCount())$
$new\_I0 \leftarrow AdcRawToVoltage(adc\_0.measure())/R_{sense}$
$new\_I1 \leftarrow AdcRawToVoltage(adc\_1.measure())/R_{sense}$

if $magnetic\_sensor\_data\_ready == True$ **then**
    $magnetic\_sensor\_data\_ready == False$
    $raw\_data = magnetic\_sensor.ReadData()$
    $sensor\_data = magnetic\_sensor.ConvertData(raw\_data)$
    $magnetic\_sensor.StartMeasurement()$
end if
$force\_data = HalToForce.convert(sensor\_data)$
if $state == stop$ **then**
    $motor\_0.SetOutput(0)$
    $motor\_1.SetOutput(0)$
else if $state == calibrate$ **then**
    if $motor\_0.IsCalibrating()$ **then**
        $calibrator\_0.Update(motor\_0, new\_pos\_0, encoder\_0)$
    else if $motor\_1.IsCalibrating()$ **then**
        $calibrator\_1.Update(motor\_1, new\_pos\_1, encoder\_1)$
    else
        $state = position$
    end if
else if $state == position$ **then**
    $motor\_0.SetOutput(positionPID(new\_pos\_x, des\_pos\_x))$
    $motor\_1.SetOutput(positionPID(new\_pos\_y, des\_pos\_y))$
else if $state == torque$ **then**
    $force\_action\_0 = forcePID(force\_data.x, f\_des\_x)$
    $force\_action\_1 = forcePID(force\_data.y, f\_des\_y)$
    if $(force\_data.z < no\_load\_force)\&(min\_pos\_0 + 0.25 < new\_pos\_0 < max\_pos\_0 - 0.25)$ **then**
        $motor\_0.SetOutput(force\_action\_0)$
    else
        $motor\_0.SetOutput(0)$
    end if
    if $(force\_data.z < no\_load\_force)\&(min\_pos\_1 + 0.25 < new\_pos\_1 < max\_pos\_1 - 0.25)$ **then**
        $motor\_1.SetOutput(force\_action\_1)$
    else
        $motor\_1.SetOutput(0)$
    end if
end if

The haptic control loop operates on a separate core at 500 Hz, matching the frequency of the communication loop. On every iteration, it collects data from the encoders and the current sensing circuitry of the motor drivers. Then, data is read from the magnetometer, if available, indicated by a flag toggled by the data-ready (DRDY) signal of the sensor. The selected frequency should ensure the availability of a sample on every iteration. Then, based on the current state of the system — i.e. stopped, calibrating, position control, or force control —, a control action is commanded to the motors using the current and desired position or forces. The details of the operation of the loop can be found in Algorithm 2.

The *calibrator_0* and *calibrator_1* objects in Algorithm 2 perform the blind calibration of the actuators. This is done by displacing the mechanism to the limit of the range of motion, detected by a drop in the velocity measured by the encoders. The object operates as a finite-state machine (FSM) in which each state has an associated control action, as depicted in Figure D.2. The control actions and state transition thresholds have been determined on an experimental basis to ensure a consistent and reliable response.

The FSM can be configured to determine only the lower bound of the range of motion, or both the lower and upper bound, whenever the range of motion of the actuator is unknown. Furthermore, by comparing the measured range with a known estimate, issues due to external perturbations or blocked actuators can be detected. A time limit in the speed onset is introduced to account for the possibility that the mechanism is already close to the lower end of the range of motion and the transition to the moving state is not triggered. Finally, the movement of the actuator is initiated with a high value of the control action. This was done to ensure that the actuator would overcome the static friction in the system and start displacing in the desired direction. The lower control action while moving allows the mechanism to reach the ends of the range of motion without jamming.

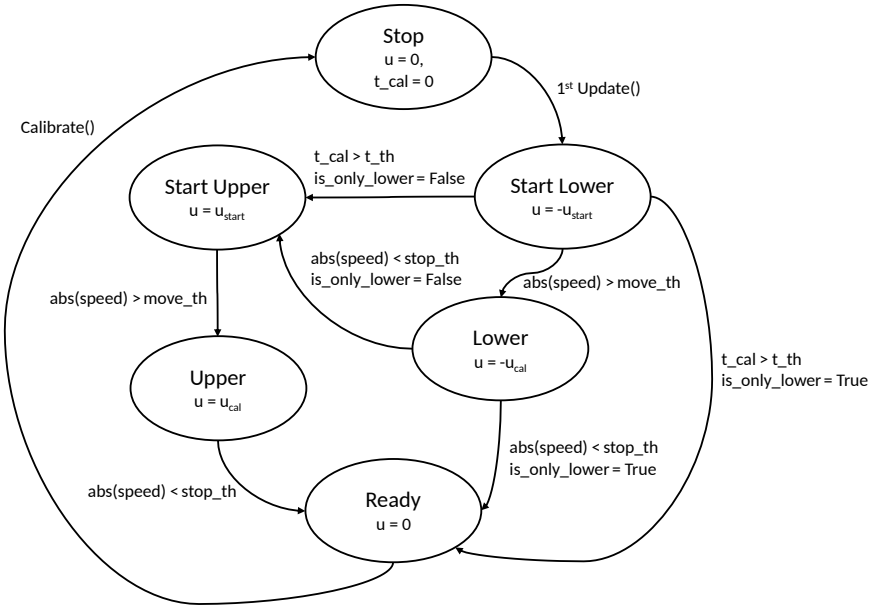

Figure D.2: State machine of the calibration procedure. u_{start} and u_{cal} correspond to the control action applied at the beginning of the displacement and once the actuator is moving. *move_th* and *stop_th* represent the velocity threshold above and below which the system is considered to be moving, or stopped at the actuation limit, respectively. *t_th* is the time after which it is considered that the actuator has reached the lower actuation limit without surpassing *move_th*.

E

Details on data acquisition

The present section aims to provide further information on the setup and steps followed to perform the calibration of the soft magnetic sensor and the force-controlled haptic device.

E.1. Experimental setup

The setup used for collecting the data necessary to calibrate and characterize the force sensor was the same one used for validating the response of the force-controlled system. A manual three-axis positioning stage was manufactured in-house using the tools described in chapter 2.

The ATI Nano 43 (ATI Industrial Automation, United States) was attached to the vertical stage using different 3D-printed mounting connectors. The measured system, either the standalone sensor or the interface, was connected to the X-Y positioning table using 3D-printed mounting racks. The connectors were designed to align the measurement axes of the two sensors.

The measurements from the ATI Nano were collected through a USB-6351 data acquisition board (National Instruments, United States), connected to the Interface Power Supply Box of the sensor, and to the USB port of the computer. Measurements from the acquisition board were collected using a Python script relying on the *nidaqmx* package and the calibration data provided by the manufacturer of the sensor. The data from the magnetic-based sensor was collected through the serial port using the *pyserial* and *json* packages.

The data from both the ATI Nano 43 and the magnetic-based sensor was collected on two separate threads initiated simultaneously. Doing so ensured that the collected data was synchronized in the time domain. Measurements from both sensors were collected at 100 Hz for the measurements on the standalone sensor, and at 500 Hz for the measurements performed on the tactile interface.

E.2. Data collection for magnetic force sensor calibration and static evaluation

A protocol document was created to ensure the correct execution of the data acquisition for calibrating the magnetic force sensor and evaluating the performance of the different mappings. In addition to facilitating the reproducibility of the results, the protocol is also meant to serve as a guideline for the calibration of future units of the sensor. The protocol can be found in Appendix G and it is meant to be used with the calibration script previously mentioned. The steps to follow are indicated, together with the expected output and additional instructions on troubleshooting potential issues during the process. When collecting data from the sensor mounted in the mechanism, no power needs to be supplied to the motors.

The target positions of the stage used to apply different forces to the sensor consist of a comprehensive sweep along the cylindrical coordinate frame of the sensor, as indicated in chapter 2. The target positions were scanned such that displacements would first occur along the radial dimension, then along the angular, and finally along the depth dimension. The target positions and scanning order are depicted in Figure E.1. Displacements were applied consecutively without moving the platform back to the initial position due to the long duration of the manual data acquisition. For the collection of samples for evaluating the generalization of the mapping, on the contrary, the position of the stage was always reset between samples.

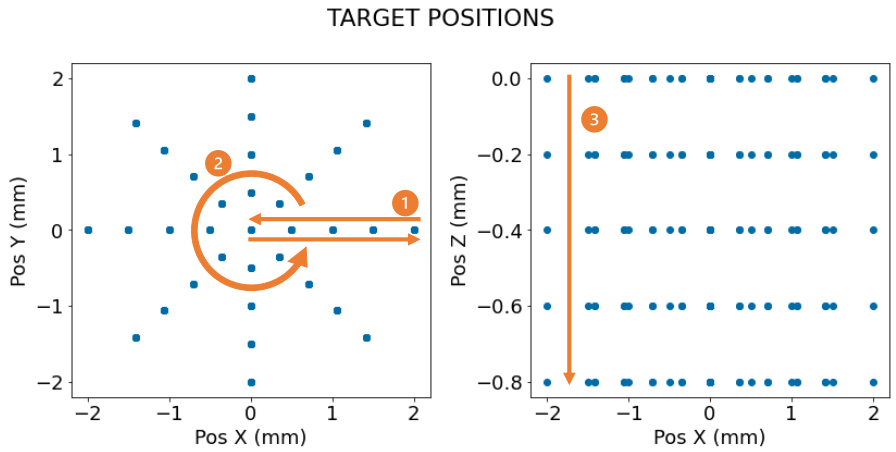

Figure E.1: Target positions used for collecting the data required for calibrating the magnetic-based force sensor. The positions cover a range of displacements along the radial, angular, and vertical dimensions to cover a sufficient range of forces of the sensor. The samples were scanned starting from the positive X semiaxis with a zero indentation in the vertical direction.

The Python script developed for collecting the calibration and evaluation data prints information on the terminal to guide the user throughout the process, in combination with the aforementioned protocol document. The script handles several errors that can arise during execution, ensuring that partially collected data can be stored under most circumstances. Thus, the script also allows resuming the collection from a certain sample so that partially collected data can be used. An overview of the workflow of the Python script for the collection of data for the calibration and static evaluation of the sensor is depicted in Figure E.2.

E.3. Data collection for single-shot measurements

The datasets for the continuous force evaluation of the sensor, the sensor characterization, and the evaluation of the performance of the force-controlled system, all comprised a single stream of continuous data from both sensors. The procedure for collecting such data was similar to the initial steps of the calibration data collection.

After initializing the communication channels and computing the bias of the ATI Nano 43 sensor, data from both sensors is displayed. Then, the user is prompted to connect the sensors, after which data from the Hall-effect sensor is displayed. This process corresponds to the first six steps depicted in Figure E.2. After that, the user is prompted to press ENTER to start the collection of the single stream of data. Finally, the data is saved to a CSV file. In a similar way to the calibration data collection, data from the sensors are collected in parallel on separate threads, ensuring the synchronicity of the data.

E.3.1. Considerations when attaching the mechanism for data collection

Many operating systems automatically toggle the Data Terminal Ready (DTR) and the Request To Send (RTS) signals upon opening and closing the serial port, sometimes overriding the settings of the software packages. The toggle of those signals causes the ESP32 to reboot, triggering the calibration of the mechanism.

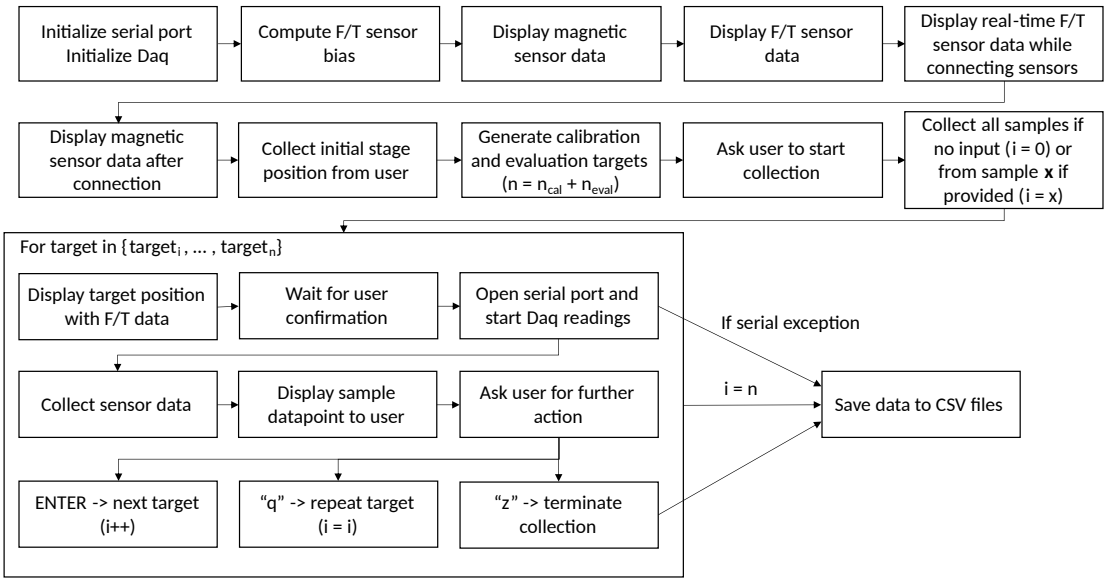

Figure E.2: Workflow of the calibration script and overall calibration procedure. Data from the Force/Torque sensor is displayed in real-time when performing the connection of the sensors and adjustments to the stage so that the measurement ranges of the sensor are not surpassed. The collection terminates upon complete data collection or premature termination due to a serial error or user request, always saving collected data to CSV files.

The files for the validation of the system response feature an additional prompt requesting the user to disconnect the ATI Nano 43 from the mechanism before terminating the execution. Doing so prevents the system from calibrating while the ATI Nano 43 is attached, which can lead to damage to the components and the sensor. Alternatively, a version of the embedded software that skips the calibration can be uploaded to the microcontroller.

E.4. Connectors for platform rotations

In order to perform the tests to evaluate the impact of platform rotations on the measurements of the magnetic-based sensor, modified connectors for the F/T sensor were designed. Said connectors are designed to align with the connector of the standalone sensor once a rotation of 15° is applied. Figure E.3 shows the CAD model of the connectors for each axis. Note that due to the layout of the mounting screws in the F/T sensor, the connectors for the X and Y axes have to be different and cannot be rotated 90°.

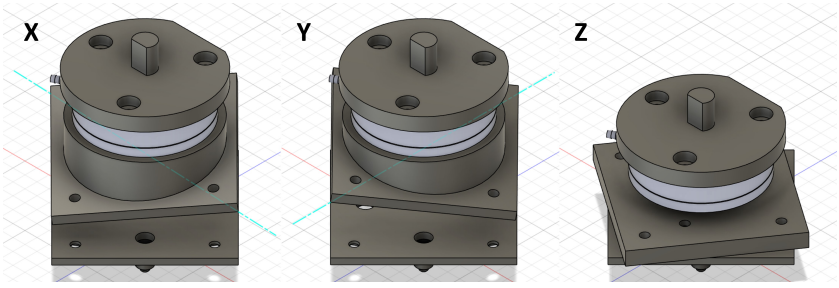

Figure E.3: Modified connectors for the F/T sensor to measure the impact of rotations on the measurements of the magnetic-based sensor. The panels depict the connectors, from left to right, around the X, Y, and Z axes.

F

Supplementary results

This appendix presents additional information on the evaluations and measurements conducted on the system. While the main findings are provided in chapter 2, the sections in this appendix provide additional information and visualizations for the tests performed in the study. Those tests for which all necessary information is considered to be provided in the body of the study are not touched upon.

F.1. Sensor calibration and evaluation

When performing the calibration and evaluation of the magnetic-based sensor, an initial analysis of the data from both the magnetometer and the F/T sensor was carried out. Figure F.1 shows the raw data from both sensors along different pairs of axes. It can be observed that the magnetic field and the applied forces follow a rather linear relationship along the X and Y axes. The magnetic field readings around X and Y span over the measurement range of the magnetometer over a total range of approximately 10 mT. The corresponding forces cover a range of 8 N along each semiaxis.

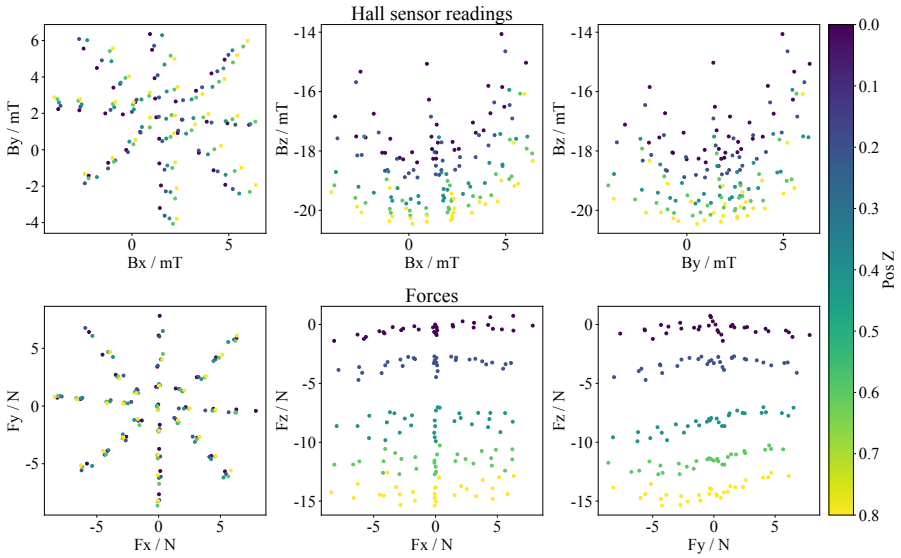

Figure F.1: Samples of magnetic field data measured by the magnetometer of the standalone sensor unit, and force data from the reference F/T sensor. The color scale corresponds to the position of the stage along the Z axis. Each point in the scatter corresponds to the average of the 100 data points collected at each deformation of the elastomer.

When inspecting the forces along the Z axis, large changes in the intensity of the magnetic field due to shear forces can be observed. Those changes are of similar magnitude as the variations in intensity resulting from the forces on the Z axis, about 2 mT. Due to the small size of the sensor, the strength of the magnetic field changes abruptly when moving off-axis.

The raw data was preprocessed as discussed in chapter 2. The bias was obtained by visual inspection of the raw data, although future versions should attempt to perform a numeric calculation of this value. As discussed in chapter 2, we calibrated and evaluated different combinations of degrees of polynomial expansions and mappings of the magnetic field to forces. Further inspection of the performance of the selected model, the Huber regression on an order 3 polynomial, was carried out. Figure F.2 shows the distribution of the errors made by the trained model over the applied force during the calibration and the evaluation. It can be observed that the errors have a similar magnitude over the range of forces applied during the calibration and evaluation, and no overall bias or offset. It can also be noticed that in the Z axis, small vertical clusters of data points can be observed. These correspond to data points belonging to the same deformation. The relatively large difference between those data points highlights the sensitivity of the model to variations in the magnetic field along the Z axis. Finally, the fact that such variations arise throughout data continuously collected at 100 Hz indicates that stray magnetic field noise is the most likely cause for such variations.

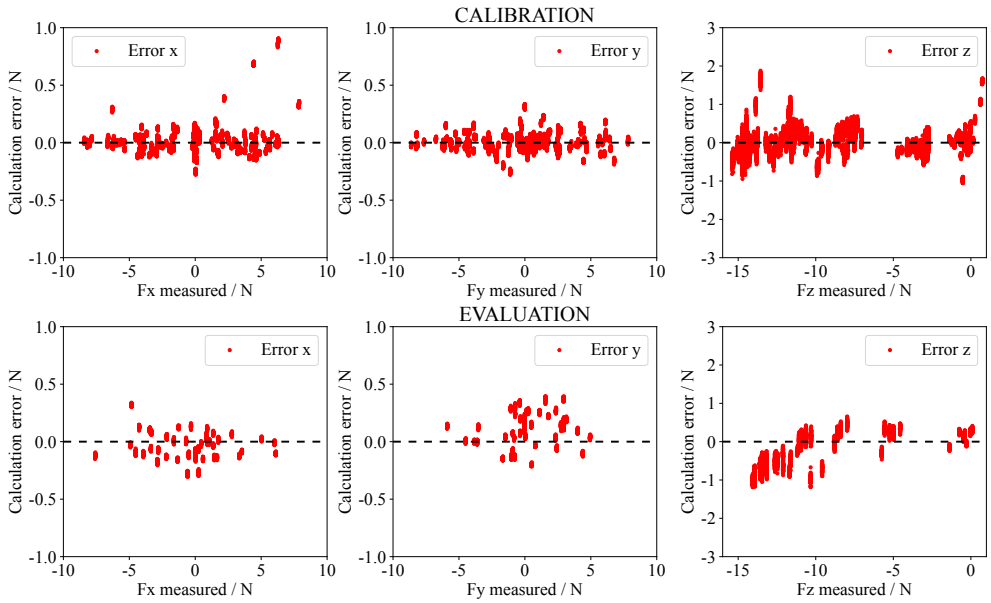

Figure F.2: Errors performed by the trained mapping on the calibration and evaluation data with respect to the applied force. The graphs show the errors of all data points of the datasets along each of the measurement axes of the sensor.

F.2. Impact of platform rotations

For the computation of the impact of platform rotations around each axis, the measurement error during no-load conditions was calculated and compared with the measurement error once the rotation had been applied to the sensor. Table F.1 gathers the measurement errors in the magnetic-based sensor at the start of the collection (no-load conditions) and at the end of the collection (once the rotation was applied). The three-dimensional MAE at those two moments is also reported, which was calculated as the L2 Norm of the error along each axis. The final impact of the rotation is then computed as the variation in three-dimensional MAE between the no-load and rotated conditions. Additional graphs showing the temporal evolution of the applied and measured forces during the rotation of the platforms are provided in Figure F.3.

Table F.1: Metrics extracted from the analysis of the impact of platform rotations on the force measurements. The 3D MAE corresponds to the L2 Norm of the MAE per axis. The variation computed in the last column is computed as the difference in 3D MAE.

	MAE start / N			**MAE end** / N			**3D MAE** / N		
Rotated axis	**X**	**Y**	**Z**	**X**	**Y**	**Z**	**Start**	**End**	**Variation** / N
X	0.091	0.171	0.662	0.020	1.561	5.588	0.690	5.802	5.113
Y	0.111	0.219	0.644	1.438	0.412	7.182	0.689	7.337	6.647
Z	0.166	0.243	0.920	0.367	0.106	1.763	0.965	1.804	0.839

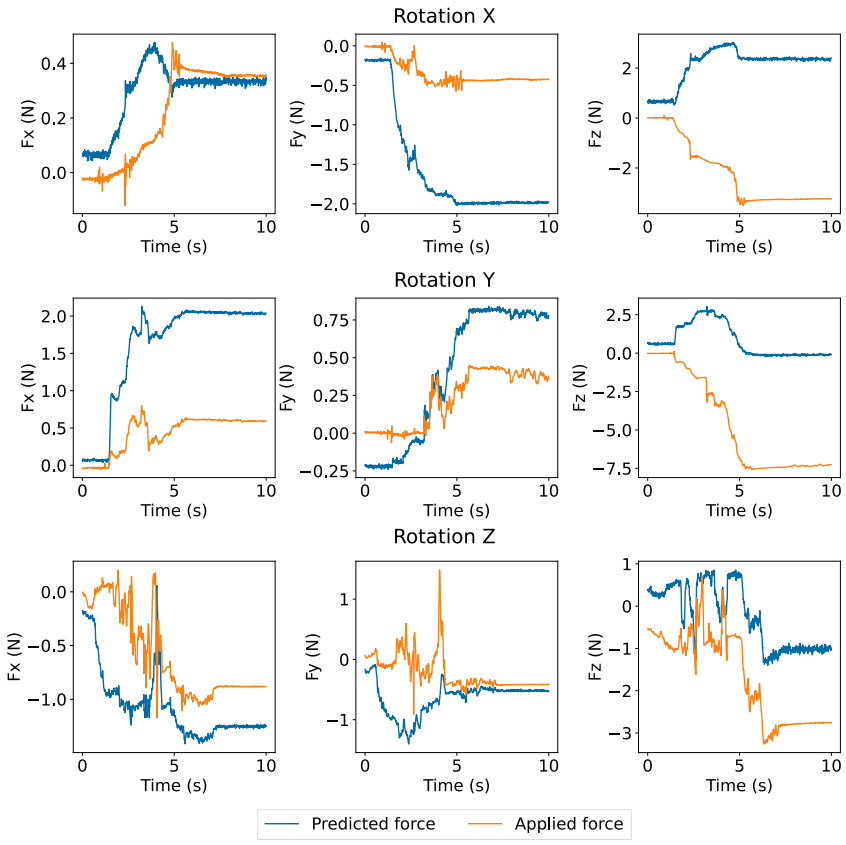

Figure F.3: Temporal evolution of the applied and measured forces during the rotation of the platforms during the test.

F.3. Step response evaluation

The response of the system under all of the commanded steps is depicted in Figure F.4, and a detailed view from a sample step along each direction is presented in Figure F.4. Notice that a small period of no collected data was taken between steps to ensure the synchronicity of the data for each step. A ripple is observed in the diagonal direction for steps of 1 N and 2 N amplitudes.

In addition to the final metrics presented in chapter 2, the values were also extracted for each amplitude and each direction to investigate potential amplitude- and direction-dependent variations. The resulting metrics are gathered in Table F.2 and Table F.3. It can be observed that the rise time is roughly constant throughout the ranges of forces inspected and across directions.

The steady-state error measured by the magnetic-based sensor shows consistently low values for all directions and amplitudes. When looking into the steady-state error computed from the data of the F/T sensor, much larger errors are observed. The magnitude of those errors is larger for the Y direction. In all directions, the magnitude of the error increases with the amplitude of the step signal commanded. However, the increase is not proportional to the amplitude of the step but increases about 0.08 N/N in the X direction, 0.120 N/N in the Y direction, and about 0.09 N/N in the 45° direction.

While the overshoot measured by the magnetic-based sensor takes very small values, the magnitude of the overshoot measured by the F/T sensor is much larger. When comparing across amplitudes, the overshoot decreases as the amplitude of the step increases, due to the increased stress in the elastomer, which dampens the movement of the actuators.

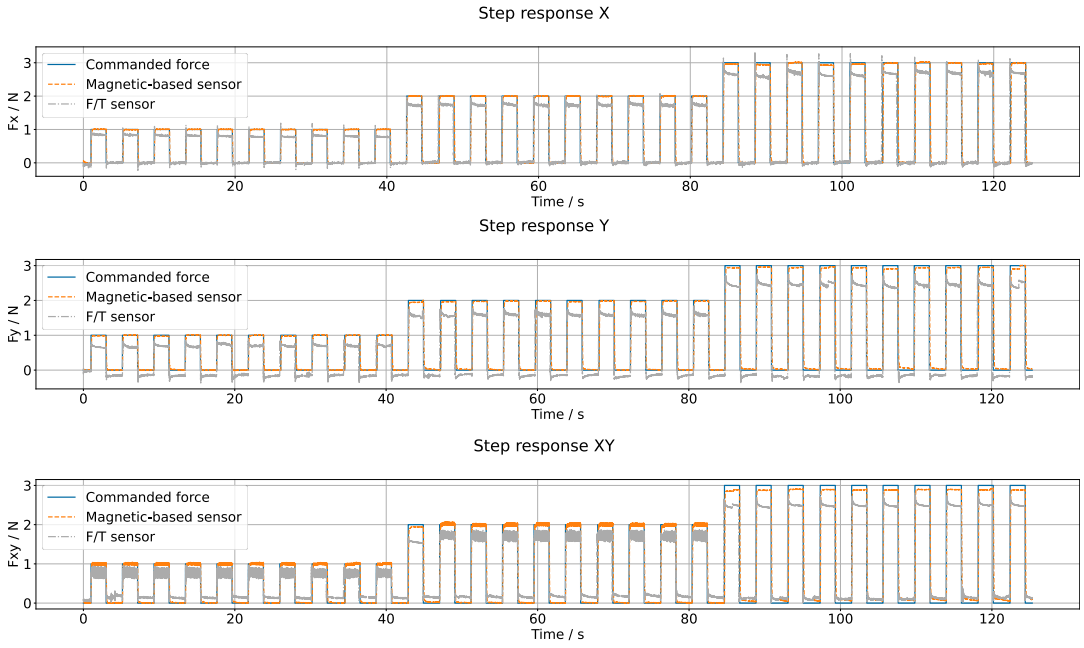

Figure F.4: Temporal evolution of the step response of the system during the step response test along the X, Y, and 45° (XY) directions.

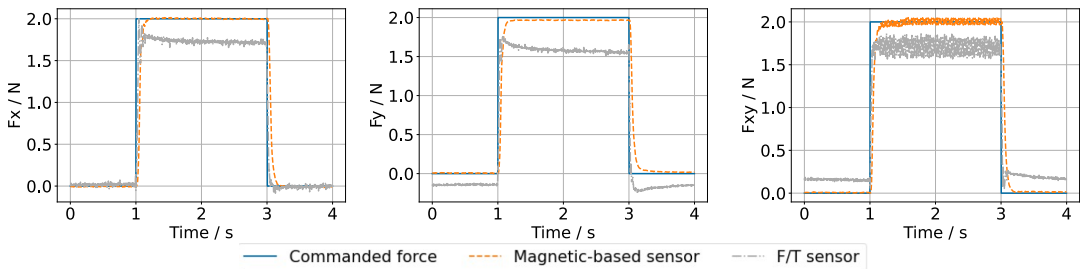

Figure F.5: Examples of a step response of the system along the X (left), Y (center), and 45° (right) directions.

Table F.2: Metrics extracted per direction and amplitude during the step response tests from the magnetic-based sensor data. SSE states for steady-state error.

	Magnetic-based sensor								
	Rise time / s			**SSE /** N			**Overshoot /** %		
Direction	**1N**	**2N**	**3N**	**1N**	**2N**	**3N**	**1N**	**2N**	**3N**
X	0.054	0.069	0.064	0.002	0.004	0.032	1.077	0.759	0.000
Y	0.060	0.065	0.069	0.011	0.028	0.051	0.589	0.000	0.000
45°	0.078	0.075	0.061	0.006	0.014	0.108	3.873	1.904	0.000

Table F.3: Metrics extracted per direction (rows) and amplitude (columns) during the step response tests from the F/T sensor data. SSE states for steady-state error.

	F/T sensor								
	Rise time / s			**SSE /** N			**Overshoot /** %		
Direction	**1N**	**2N**	**3N**	**1N**	**2N**	**3N**	**1N**	**2N**	**3N**
X	0.019	0.025	0.035	0.199	0.279	0.358	39.357	16.573	20.693
Y	0.008	0.018	0.029	0.320	0.440	0.565	25.796	13.559	12.562
45°	0.104	0.023	0.024	0.243	0.315	0.528	25.198	9.606	11.863

F.4. Frequency response evaluation

The raw data gathered from the frequency response test was first inspected in the time domain. The resulting responses are depicted in Figure F.6. Both sensors showed similar measures of the response of the system, which achieves good tracking at lower frequencies before attenuating due to the high frequency of the commanded signal.

When comparing the measured responses by the two sensors, it can be observed that the response attenuates at lower frequencies for the X axis than for the Y axis, attributed to the larger mass moved by the system in the X direction. Additionally, it can be observed that the low number of targets generated for the high-frequency parts of the commanded signal resulted in a drift in the force generated along the Y axis. Finally, it can be noted that tracking performance at low frequencies is qualitatively better in the Y axis, while in the X axis the system struggled to reach the maximum values of the commanded signal.

It can also be noticed how both responses exhibit an overall offset in the measurements of the magnetic-based sensor with respect to the F/T sensor. While in the Y axis this offset was uniform throughout the stream of data, in the X axis it was more prominent at higher frequencies. The reason for these offsets was attributed to deviations in the measurements of the sensor and the friction between the platform and the housing of the interface, as discussed in chapter 2.

Finally, the amplitude of the forces recorded by the magnetic-based sensor at the resonant frequency was smaller than those recorded by the F/T sensor. This was attributed to the first-order low-pass filter applied to the magnetic-based sensor measurements and the reduced temporal resolution of the magnetic-based sensor (running at maximum measurement rate) with respect to the F/T sensor (capable of up to 10kHz measurements).

When computing the amplitude of the signal as a function of the frequency, however, the observed response was found to differ from the raw temporal data, showing a continuously decreasing magnitude instead of the resonance observed in the temporal response (see Figure F.7). Further analysis of the frequency response of the commanded signal showed that even though the amplitude of the chirp was kept constant all through the frequency range, the effective amplitude decreased as a function of the frequency.

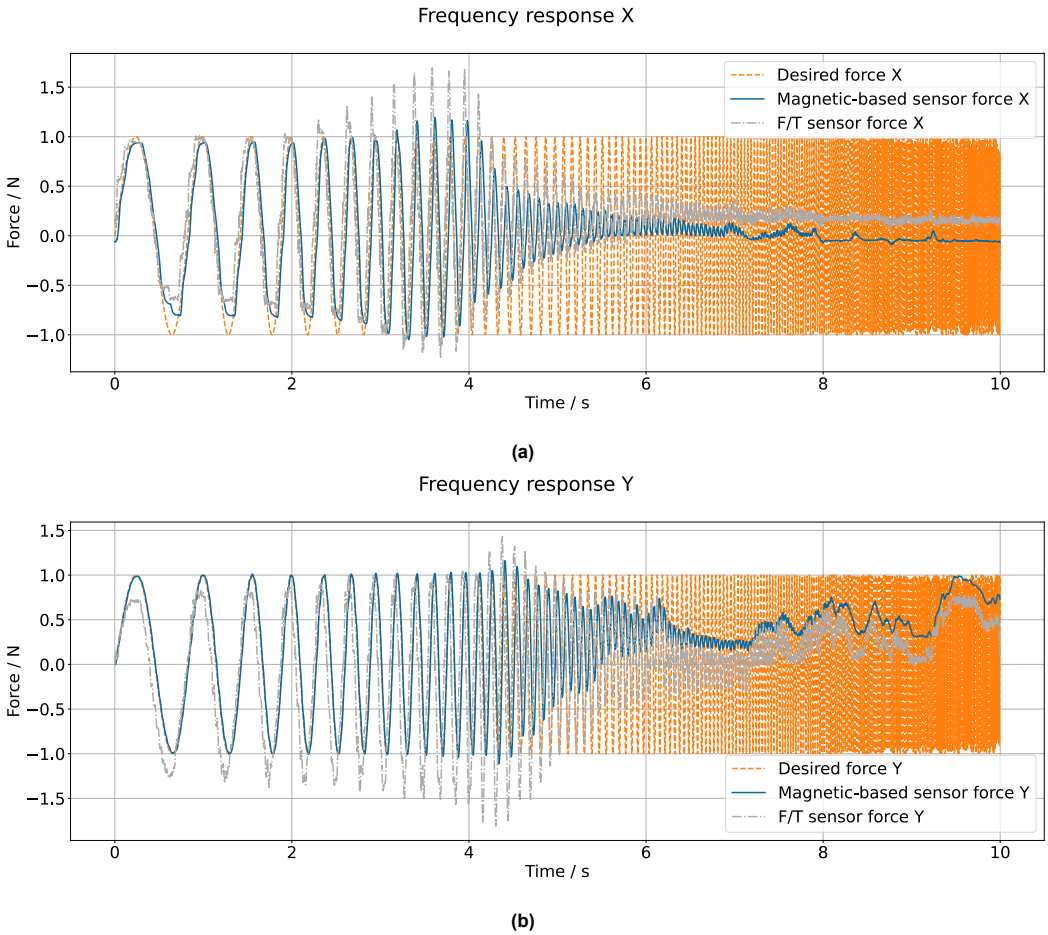

Figure F.6: Frequency response of the system in the time domain when commanded an exponential chirp signal sweeping from 1 Hz to 100 Hz along the X axis (top) and Y axis (bottom). The commanded signal and responses recorded by the magnetic-based sensor and the F/T sensor are displayed.

Such a decrease was attributed, on the one hand, to the under-representation of the signal caused by the sampling, which could also be appreciated in the form of clipping at high frequencies in Figure F.6. On the other hand, the continuous and exponentially increasing change in the frequency of the commanded chirp signal resulted in smaller data collected for each of the high-frequency components. The choice of the exponentially increasing sweep rather than a linear one was to obtain greater insights into the response of the system at the frequencies most relevant during normal operation, rather than collecting more data in highly-attenuated regions.

Upon these observations, the response of the system was then quantified as the gain of the system with respect to the commanded signal. Thus, the gain was computed as the ratio between the magnitude of the response and the magnitude of the commanded chirp signal, resulting in the graphs shown in chapter 2.

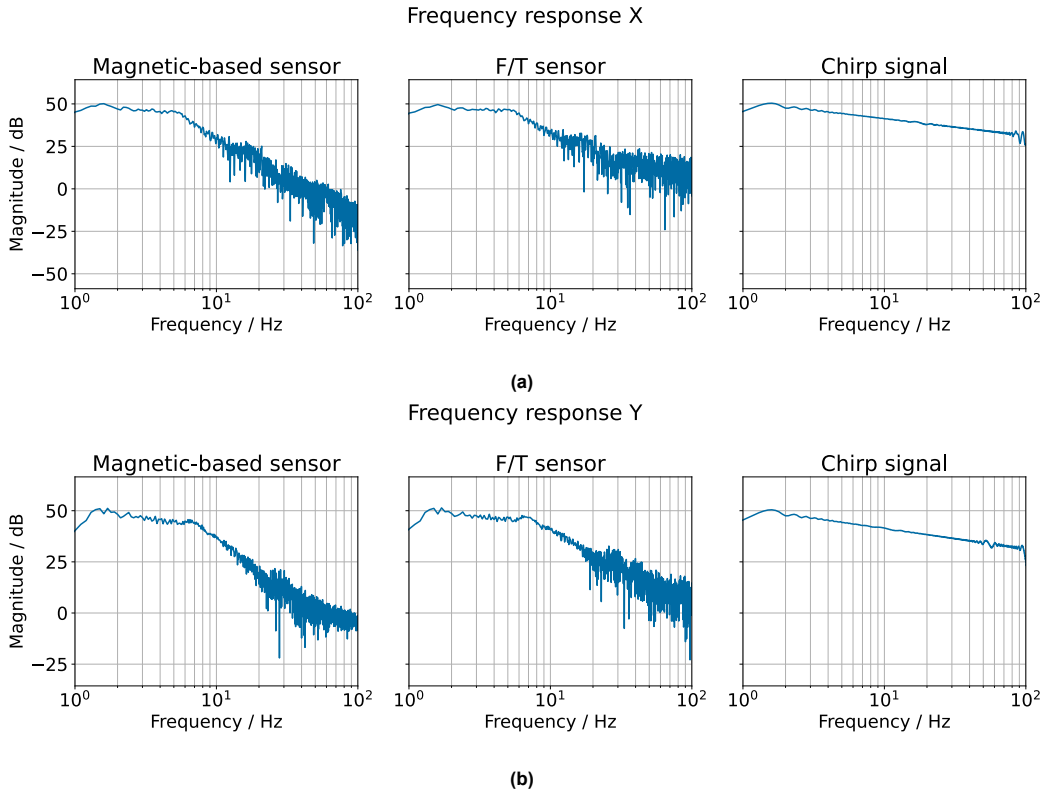

Figure F.7: Magnitude response of the system along the X axis (a) and Y axis (b). The magnitude of the signal for the analyzed frequencies is displayed. The panels of each subfigure response depict the response measured by the magnetic-based sensor (left), the response measured by the F/T sensor (center), and the commanded chirp signal. Despite the constant amplitude of the signal, the effective amplitude of the signal was found to reduce for high-frequency components.

G

Technical documents

This chapter contains the technical documents generated for different components of the developed system. These include the schematics of the PCBs and the drawings with the dimensions of the components manufactured in-house.

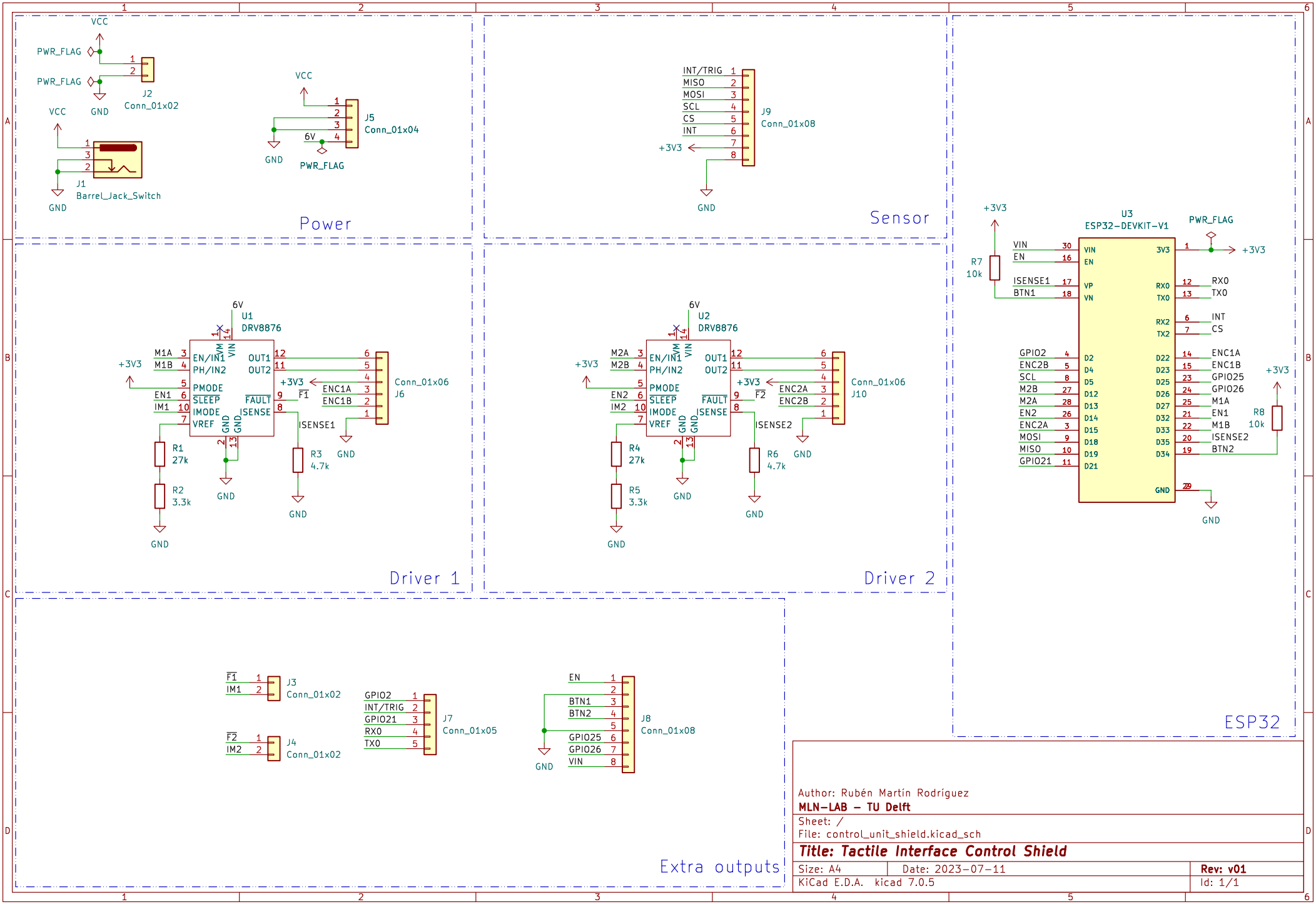

Author: Rubén Martín Rodríguez
MLN-LAB – TU Delft

Sheet: /
File: control_unit_shield.kicad_sch

Title: Tactile Interface Control Shield

Size: A4	Date: 2023-07-11	**Rev: v01**
KiCad E.D.A. kicad 7.0.5		Id: 1/1

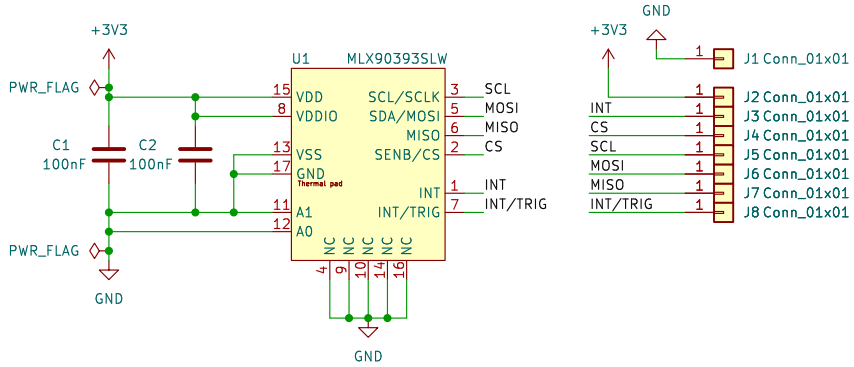

Author: Rubén Martín Rodríguez
MLN-LAB – TU Delft

Sheet: /
File: mlx90393_force_sensor.kicad_sch

Title: MLX90393 Force sensor

Size: A4	Date: 2023-07-11	**Rev: v01**
KiCad E.D.A. kicad 7.0.5		Id: 1/1

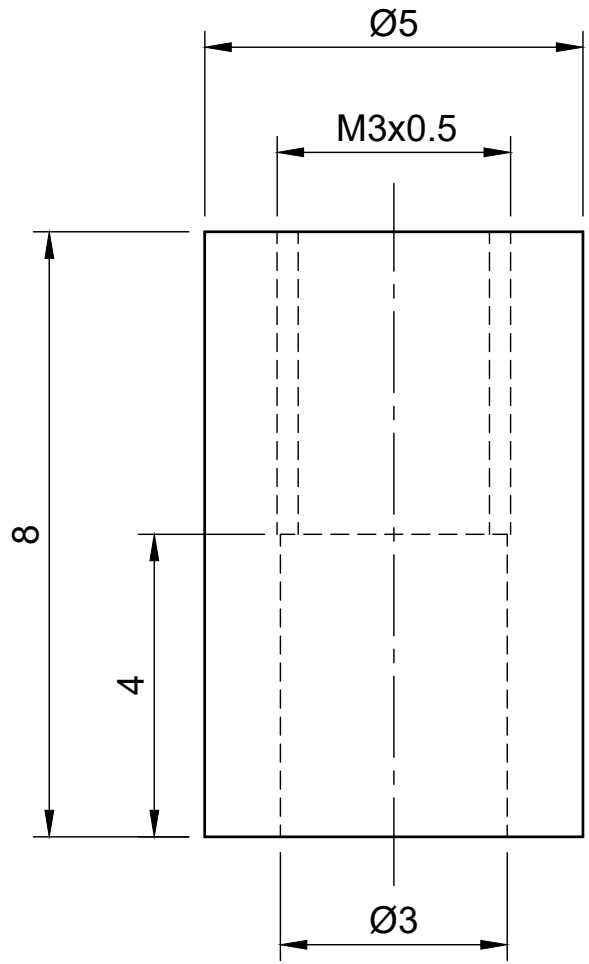

Dept.	Technical reference	Created by	Approved by
CoR-MLN	-	Ruben Martin Rodriguez 16-May-23	Ruben Martin Rodriguez 16-May-23
Scale: 10:1		Document type: Technical drawing	Document status: -
		Title: Homemade_coupler	DWG No.: 1
			Rev.: 01 / Date of issue: 02-09-2023 / Sheet: 1/1

Part list	
1	Leadscrew
2	Coupler
3	DC motor
4	Encoder
5	Magnetic disk

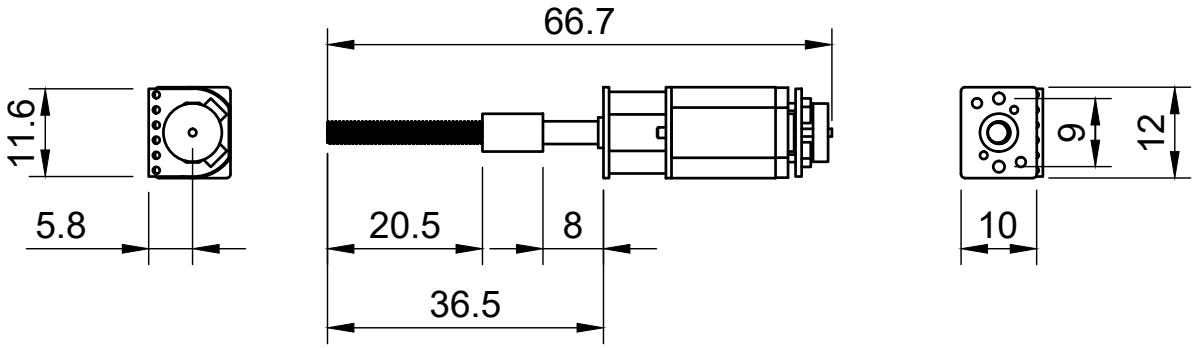

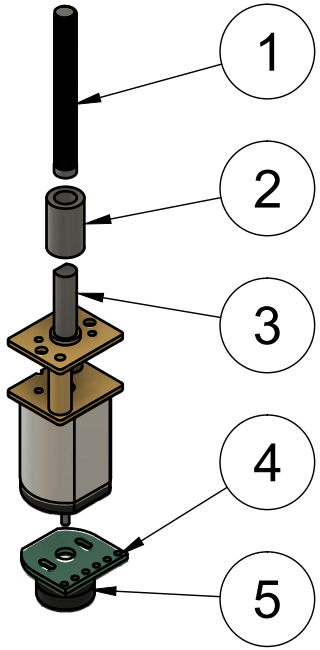

Dept.	Technical reference	Created by	Approved by
CoR-MLN	-	Ruben Martin Rodriguez 02-Sep-23	Ruben Martin Rodriguez 02-Sep-23
Scale: 1:1		Document type: Technical Drawing	Document status: -
		Title: Linear actuator	DWG No.: 2
			Rev.: 01 / Date of issue: 02-Sep-23 / Sheet: 1/1

Protocol on calibration of the magnetic-based 3-axis force sensor

Materials

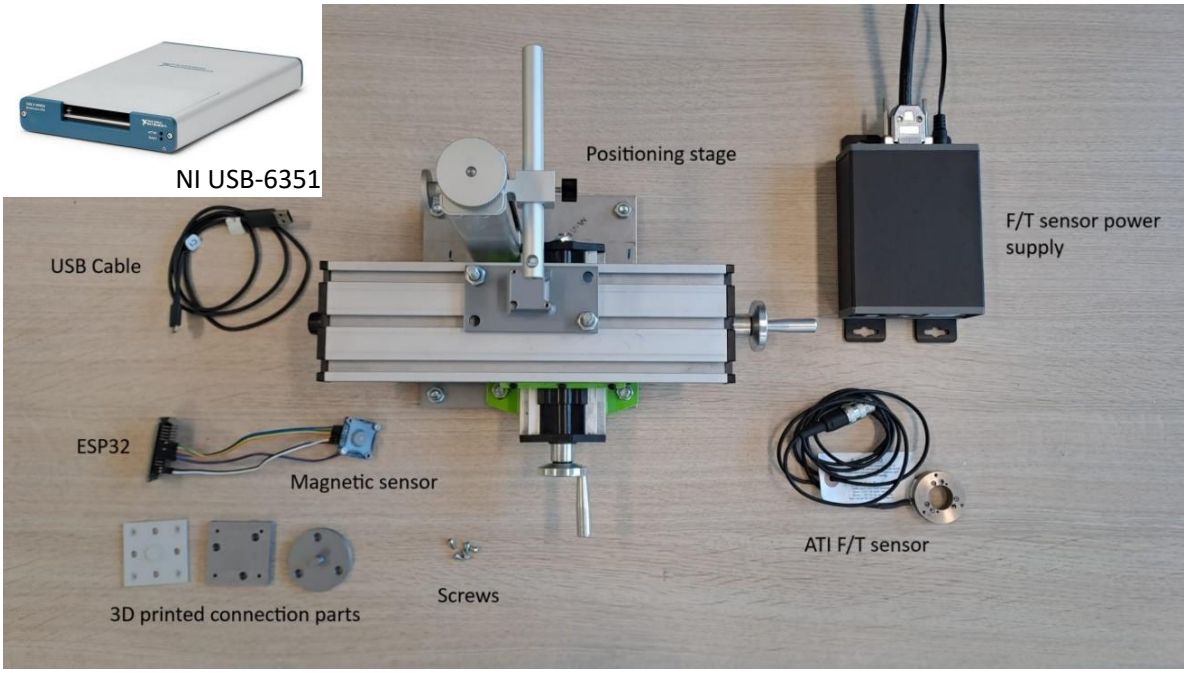

• ATI Nano 43 force sensor with power supply and data acquisition system.	☐
• Magnetic sensor (either using an evaluation board or custom system), connected to ESP32 for interfacing.	☐
• 3D-printed parts for attaching the sensor to the calibration stage and the magnetic sensor (may need to be tailored to stage and calibrated system). Additional hardware:	☐
○ 6x M3x4/5mm screws	☐
○ 4x M3x8mm screws	☐
○ 4x M3 nuts	☐
• 3-axis calibration stage with displacement scales	☐
• Computer with:	☐
○ Support for reading ATI Nano sensors (NI PCIe-6323 DAQ or NI USB-6351)	☐
○ USB 3.0 port for ESP32	☐
○ Python with necessary packages:	☐
▪ nidaqmx	
▪ numpy	
▪ pandas	
▪ json	
▪ pyserial	
• Scripts for reading data:	☐
○ tools.py	
○ calibration_script.py	
○ ati_communication.py	

Preparations

• Mount the system with the magnetic sensor and the ATI Nano in the two parts of the calibration stage with relative motion on the three axes. This will depend on the calibration stage. Connect the sensor depending on the selected DAQ.
  ○ DO NOT CONNECT THE ATI Nano TO THE MAGNETIC SENSOR YET
  ○ MAKE SURE THAT THE +X AXES OF THE SENSORS ARE ALIGNED
  ○ A reference image using a custom calibration stage, an EVB90393, and an ATI Nano sensor is shown below. An image of the ATI connected through a NI USB-6351 is also shown
 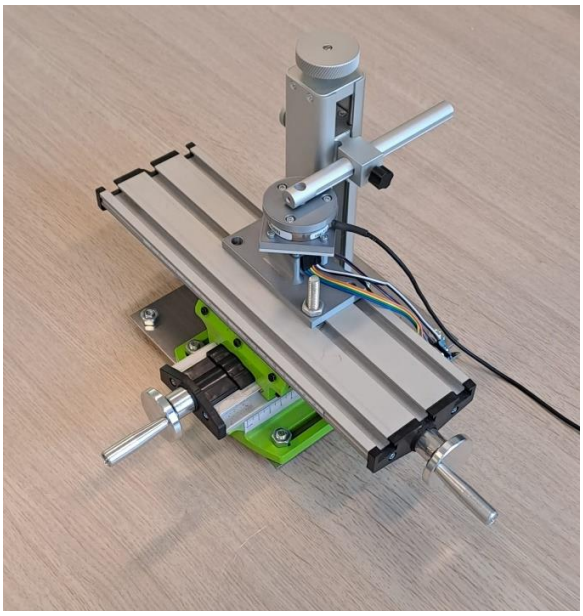 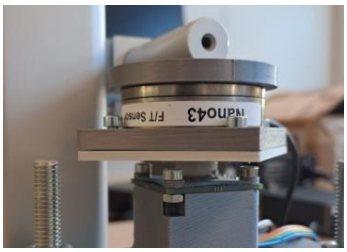 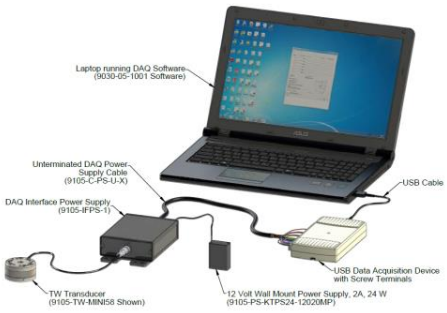
	☐

• Connect the ESP32 to the computer using a compatible USB cable.	☐
• Make sure that the ATI Nano sensor is connected to the data acquisition card of the computer.	☐
• Verify that the sensor is connected and working properly using the ATIDAQFT.Net program that should be installed on the computer. Alternatively, the calibration script will display some data upon starting to verify that the readings are correct.	☐
• If not done already, create a folder for the project (e.g., *calibration*) and place the Python scripts in an additional folder within it (i.e., within *calibration/python*). • A **data** folder can also be created in the project folder (i.e., *calibration/data*) to store the data from the calibration. Otherwise, it will be automatically created.	☐
• Make sure that the ATI Nano sensor is attached to the 3D printed parts and to the linear stage. The ATI sensor **MUST NOT** be connected to the magnetic sensor upon initialization to adequately bias it.	☐
• Open the IDE or terminal to run Python. Notice that you may need to change the serial port to which the ESP32 is connected (COMx). Execute the **calibration_script.py** file.	☐

Data collection

• Data from the magnetic sensor will be displayed, followed by *"Press ENTER to continue"*.
  ○ Press **ENTER** if the data is nonzero and in the range of [-10000, 10000]. Otherwise, interrupt execution using **CTRL+C** and debug any issue with the ESP32.
  ○ Sometimes, upon the first connection, the board sends initialization data that can result in no sensor readings displayed. Can interrupt (**CTRL+C**) and restart, or move on, since actual data will be available by the time collection starts.
	☐

• Calibrated data from the ATI Nano will be displayed on the terminal, followed by *"Press ENTER to continue"*. ○ If the readings are close to zero in all axes, press **ENTER** to continue. Otherwise, use **CTRL+C** to interrupt the execution and debug any issues with the ATI sensor.	☐
• Connect the sensors using the M3 screws. Move the linear stage to ensure that the readings from the ATI Nano displayed on screen are as close to zero as possible. ○ Once that is the case, press **ENTER** to continue (confirmation will be requested).	☐
• Enter the initial positions in the X, Y and Z axes of the adjusted platform. Non-numeric or empty inputs will be disregarded. **q** can be used to repeat the last input. ○ Confirmation will be asked by pressing **ENTER**. The position of all axes can be introduced again by inputting **q**.	☐
• Text will indicate the number of targets generated for calibration and evaluation (165 and 45, respectively), followed by *"Press ENTER to start data collection, or enter sample value from which to start collection: "***.** ○ Press **ENTER** to start the data collection or introduce the sample number from which to start the collection	☐

• The procedure below will be repeated for the total number of targets generated (210).
  ○ The initial position and target position relative to it will be displayed together with real-time readings of the ATI Nano.
  ○ Adjust the stage until the position matches the target one and press **ENTER**.
  ▪ Look out for torques not to overcome a value of ±**250**, or forces to overcome ±**18**.
  ○ A message stating "*Press ENTER to collect data or press q to go back:* ".
  ▪ Press **ENTER** to collect data from the ATI Nano sensor and the MLX90393.
  ▪ To re-adjust the stage, provide "q" as an input.
  ○ Finally, one data point from the sample will be displayed, followed by "*Press ENTER to move on, q to repeat sample, z to finish collection: "*.
  ▪ Input **q** to repeat the sample (including positioning), **z** to interrupt data collection, or **ENTER** to collect the next sample
	☐
	☐
	☐
	☐
	☐

• Once all the samples have been gathered, the message *"Do you want to save the logs to a file? (y/no)"* will be displayed. It may be the case, although unlikely, that the some SerialException will occur. In those cases, an informative message will be displayed before to indicate that an exception happened and that partial data will be saved. ○ Press **ENTER** or input **y** to save the logs.	☐
• A confirmation message (*"Are you sure? (y->confirm, n->go back): "*) will pop up asking to confirm your choice. ○ Input **y** to confirm the choice and save the data.	☐
• Two CSV files will be found on the **data** folder within the project folder, starting with *data_cal_* and *data_eval_*, containing calibration and evaluation data respectively. The files will terminate with a unique identifier based on the date and time of the file creation.	☐

Bibliography

[1] Brian T. Gleeson, Scott K. Horschel, and William R. Provancher. “Design of a Fingertip-Mounted Tactile Display with Tangential Skin Displacement Feedback”. In: *IEEE Transactions on Haptics* 3.4 (Oct. 2010). Conference Name: IEEE Transactions on Haptics, pp. 297–301. ISSN: 2329-4051. DOI: 10.1109/TOH.2010.8.

[2] Théo Le Signor, Nicolas Dupré, and Gael F. Close. “A Gradiometric Magnetic Force Sensor Immune to Stray Magnetic Fields for Robotic Hands and Grippers”. In: *IEEE Robotics and Automation Letters* 7.2 (Apr. 2022). Conference Name: IEEE Robotics and Automation Letters, pp. 3070–3076. ISSN: 2377-3766. DOI: 10.1109/LRA.2022.3146507.

[3] Théo Le Signor et al. “Mass-Manufacturable 3D Magnetic Force Sensor for Robotic Grasping and Slip Detection”. In: *Sensors* 23.6 (Jan. 2023). Number: 6 Publisher: Multidisciplinary Digital Publishing Institute, p. 3031. ISSN: 1424-8220. DOI: 10.3390/s23063031. URL: https://www.mdpi.com/1424-8220/23/6/3031 (visited on 04/10/2023).

[4] Raphael Rätz, René M. Müri, and Laura Marchal-Crespo. “Design of a Haptic Palmar Device with Thumb Flexion and Circumduction Movements for Sensorimotor Stroke Rehabilitation”. In: *2022 44th Annual International Conference of the IEEE Engineering in Medicine & Biology Society (EMBC)*. 2022 44th Annual International Conference of the IEEE Engineering in Medicine & Biology Society (EMBC). ISSN: 2694-0604. July 2022, pp. 2644–2647. DOI: 10.1109/EMBC48229.2022.9871303.

[5] Raphael Rätz et al. “A Novel Clinical-Driven Design for Robotic Hand Rehabilitation: Combining Sensory Training, Effortless Setup, and Large Range of Motion in a Palmar Device”. In: *Frontiers in Neurorobotics* 15 (Dec. 20, 2021), p. 748196. ISSN: 1662-5218. DOI: 10.3389/fnbot.2021.748196. URL: https://www.ncbi.nlm.nih.gov/pmc/articles/PMC8721892/ (visited on 11/02/2022).

[6] Samuel B. Schorr and Allison M. Okamura. “Fingertip Tactile Devices for Virtual Object Manipulation and Exploration”. In: *Proceedings of the 2017 CHI Conference on Human Factors in Computing Systems*. CHI ’17. New York, NY, USA: Association for Computing Machinery, May 2, 2017, pp. 3115–3119. ISBN: 978-1-4503-4655-9. DOI: 10.1145/3025453.3025744. URL: https://doi.org/10.1145/3025453.3025744 (visited on 11/04/2022).

[7] Tito Pradhono Tomo et al. “Design and Characterization of a Three-Axis Hall Effect-Based Soft Skin Sensor”. In: *Sensors* 16.4 (Apr. 2016). Number: 4 Publisher: Multidisciplinary Digital Publishing Institute, p. 491. ISSN: 1424-8220. DOI: 10.3390/s16040491. URL: https://www.mdpi.com/1424-8220/16/4/491 (visited on 04/09/2023).

[8] Hongbo Wang et al. “Design Methodology for Magnetic Field-Based Soft Tri-Axis Tactile Sensors”. In: *Sensors* 16.9 (Sept. 2016). Number: 9 Publisher: Multidisciplinary Digital Publishing Institute, p. 1356. ISSN: 1424-8220. DOI: 10.3390/s16091356. URL: https://www.mdpi.com/1424-8220/16/9/1356 (visited on 05/26/2023).